POLITECNICO DI TORINO
Repository ISTITUZIONALE

Experimental characterization of the energy performance of an Heat Harvesting Window integrating an air to PCM latent heat exchanger

Original
Experimental characterization of the energy performance of an Heat Harvesting Window integrating an air to PCM latent heat exchanger / Li Castri, G., Raad, A., Rapone, L., Serra, V., Favoino, F.. - In: ENERGY AND BUILDINGS. - ISSN 1872-6178. - ELETTRONICO. - 371:(2026). [10.2139/ssrn.6478228]

Availability:
This version is available at: 11583/3015096 since: 2026-09-02T14:32:04Z

Publisher:
Elsevier

Published
DOI:10.2139/ssrn.6478228

Terms of use:

This article is made available under terms and conditions as specified in the corresponding bibliographic description in the repository

Publisher copyright

(Article begins on next page)

20 November 2026

Energy & Buildings 371 (2026) 118140

Contents lists available at ScienceDirect

Energy & Buildings

journal homepage: www.elsevier.com/locate/enb

Experimental characterization of the energy performance of an heat harvesting window integrating an air to PCM latent heat exchanger

Ginevra Li Castri [a], Aseel Raad [a], Lorenzo Rapone [b], Valentina Serra [a], Fabio Favoino [a,*]

[a] Technology Energy Building Environment research group, Energy Department, Politecnico di Torino, Corso Duca degli Abruzzi, 24, 10129, Turin, Italy
[b] "Power & Energy" Business Unit, WSP Italy, Via Bernina 7, 20158 Milan, Italy

ARTICLE INFO

Keywords:
Ventilated window
Phase change materials
Adaptive façade systems
Experimental energy performance assessment
Outdoor test facility

ABSTRACT

Adaptive building envelopes can enhance building energy performance by dynamically managing ventilation, solar control, and thermal storage. This paper presents the experimental evaluation of a Heat Harvesting Window (HHW), that combines a ventilated triple glazing unit with an Air to Phase Change Material Heat Exchanger (a-PCM HEX) positioned at the cavity outlet. Unlike conventional windows or Double Skin Facades, which restrict fresh air supply in Outdoor Air Curtain (OAC) or Thermal Buffer (TB) modes, or cause overheating in Supply Air mode, the HHW continuously delivers fresh air at temperature closer to thermal comfort range, by exploiting the latent heat storage. In winter Supply Air mode, median pre-heating efficiency reached 0.7–0.8 and daily heat losses were reduced by up to 90% compared with the references, mainly by lowering ventilation heat losses. In mid-season Thermal Buffer mode, the cavity efficiency exceeded unity for nearly 40% of daytime hours, indicating frequent net heat gains from passive solar buffering. In summer Outdoor Air Curtain mode, dynamic insulation efficiency was positive for over 90% of the monitored period, with an average value of 0.75, and the HHW reduced daily heat gains by more than 40%. The a-PCM HEX provided additional air-temperature moderation, including early daytime pre-cooling of about 4 °C under peak summer conditions. The study demonstrates the potential of integrating ventilated façades with latent heat storage to develop climate-responsive envelope systems capable of ensuring continuous fresh air supply and improved thermal performance.

1. Introduction

1.1. Literature review

In recent decades, the urgency to reduce greenhouse gas emissions has driven ambitious environmental goals, particularly within the European Union (EU), where the Green Deal outlines a 55% reduction in emissions by 2030 and climate neutrality by 2050 [1]. The building sector is central to this transition, accounting for approximately 40% of global energy consumption and 36% of associated CO_2 emissions. Building envelopes, and especially its transparent part, play a pivotal role in shaping both energy performance and indoor comfort conditions [2]. To address climate-specific demands and improve building performance, Triple Glazing Units (TGUs) are increasingly used even in more temperate climates, as they effectively reduce heating demand by lowering thermal losses while maintaining adequate daylight transmission [3]. Building on these advancements, researchers in recent decades have been exploring more sophisticated, multifunctional and dynamic envelope technologies that extend beyond the capabilities of state-of-the-art fenestration systems, like Double and Triple Glazing Units, including solar control and ventilation management. Among these, Double Skin Façades (DSFs) or ventilated windows have emerged as promising solutions [4,5]. A typical DSF consists of two parallel fenestration components, separated by a ventilated air cavity, which can be naturally or mechanically ventilated, and integrating shading device for dynamic solar control management [6]. Typically DSFs present only one bottom and one top opening, either on the inner or outer layer, so that the cavity ventilation can be used to covert absorbed solar radiation into heat, and either transferred from the cavity to the indoor environment (if heating needs are predominant), or removed from the cavity to the outdoor one (if instead cooling needs are exceeding heating ones) [7]. Nevertheless also more flexible versions of DSF exists, with two bottom and two top openings, so to manage the ventilation both in a more flexible way depending on varying environmental conditions, so to be able to exploit the full potential of cavity ventilation management and maximise its impact on building energy efficiency and thermal comfort [8,9]. Ventilated windows work with the same principles of DSFs, but with a narrower ventilated cavity (20–30 mm) so to host the whole thickness of the advanced transparent component within the

* Corresponding author.

https://doi.org/10.1016/j.enbuild.2026.118140
Received 23 March 2026; Received in revised form 14 July 2026; Accepted 21 August 2026
Available online 27 August 2026
0378-7788/© 2026 The Authors. Published by Elsevier B.V. This is an open access article under the CC BY-NC-ND license (http://creativecommons.org/licenses/by-nc-nd/4.0/).

Nomenclature

Symbols

A	Generic surface area, m^2
Abs_1	Solar absorptance of glazing layer 1, –
Abs_2	Solar absorptance of glazing layer 2, –
Abs_3	Solar absorptance of glazing layer 3, –
A_{glass}	Glazing area of the HHW, m^2
$c_{p,air}$	Specific heat capacity of air, J/(kg·K)
E_{in}	Total daily solar energy gain to the indoor environment, Wh
g-value	Total solar energy transmittance (SHGC), –
H_{in}	Total transmitted solar energy, Wh
$H_{v,out}$	Total incident vertical solar energy, Wh
$I_{v,in}$	Internal vertical solar irradiance, W/m^2
$I_{v,out}$	External vertical solar irradiance, W/m^2
k_{eff}	Effective thermal conductivity, W/(m·K)
$\dot{m}$	Air mass flow rate, kg/s
q	Heat flux density, W/m^2
$\dot{Q}$	Heat transfer rate, W
$\dot{Q}_{cav}$	Heat exchanged by cavity ventilation, W
$\dot{Q}_{II,in}$	Secondary heat transfer from the glazing, W
$\dot{Q}_{lw}$	Secondary (longwave) solar heat gain, W
$\dot{Q}_{pcm}$	Heat stored or released by PCM, W
$\dot{Q}_{sw}$	Shortwave solar heat gain, W
$\dot{Q}_{tr}$	Conductive heat transfer through glazing, W
$\dot{Q}_{vent}$	Ventilation-related heat exchange,
R_{se}	m^2·K/WExternal surface thermal resistance
R_{si}	m^2·K/WInternal surface thermal resistance
Rbsol	Back-side solar reflectance, –
Rbvis	Back-side visible reflectance, –
Rfsol	Front-side solar reflectance, –
Rfvis	Front-side visible reflectance, –
τ_{sol}	Solar transmittance, –
τ_{vis}	Visible transmittance, –
T	Temperature, °C
T_{cav}	Cavity air temperature, °C
$T_{cav,inlet}$	Cavity inlet air temperature, °C
$T_{cav,outlet}$	Cavity outlet air temperature, °C
$T_{hex,inlet}$	Air temperature entering the a-PCM HEX, °C
$T_{hex,outlet}$	Air temperature exiting the a-PCM HEX, °C
T_{in}	Indoor air temperature, °C
T_m	PCM melting temperature, °C
T_{out}	Outdoor air temperature, °C
T_{se}	External surface temperature, °C
T_{si}	Internal surface temperature, °C
U-value	Nominal thermal transmittance, $W/(m^2K)$
U*	Effective in-situ thermal transmittance, $W/(m^2K)$
$V_{low,vent}$	Volumetric air flow rate, m^3/s
v_{cav}	Average cavity velocity, m/s
Λ	Experimental thermal conductance, $W/(m^2K)$
ε	Dynamic insulation efficiency, –
η_{PH}	Pre-heating efficiency, –
η_{TB}	Thermal buffer efficiency–
ρ_{air}	Air density, kg/m^3
θ	Angle of incidence, °

Acronym

a-PCM HEX	Air-to-Phase Change Material Heat Exchanger
ACH	Air Changes per Hour
AOI	Angle of Incidence
CDD	Cooling Degree Days
CEN	European Committee for Standardization
CSM	Compact Storage Module
DGU	Double Glazing Unit
DSF	Double Skin Façade
EU	European Union
HDD	Heating Degree Days
HEX	Heat Exchanger
HHW	Heat Harvesting Window
HVAC	Heating, Ventilation and Air Conditioning
IAQ	Indoor Air Quality
KPI	Key Performance Indicator
LHTES	Latent Heat Thermal Energy Storage
OAC	Outdoor Air Curtain
OLS	Ordinary Least Squares
PCM	Phase Change Material
PV	Photovoltaic
SA	Supply Air
SHGC	Solar Heat Gain Coefficient
TB	Thermal Buffer
TGU	Triple Glazing Unit
TWINS	Testing Window Innovative Systems
UNI	Ente Nazionale Italiano di Unificazione
v-TGU	Ventilated Triple Glazing Unit

framing system of insulated glazing units. Ventilated windows can therefore also be used within traditional wall construction, and can have a more widespread adoption also in non fully glazed commercial buildings.

Since the early 2000s, DSFs and ventilated windows have been widely investigated, through both simulations and experimental studies. Previous works have shown that these systems can reduce surface temperatures and solar gains, and support pre-heating or pre-cooling effects; however, their performance is strongly affected by outdoor conditions, airflow controllability, façade orientation and ventilation strategy [10–13]. The behaviour of ventilated façades and DSFs is also influenced by design variables, such as cavity depth, glazing type, shading properties and thermal mass, as well as by operational variables, including climatic boundary conditions and control strategies for shading and cavity ventilation [14]. A comprehensive parametric study conducted by Alberto et al. [15] have further identified the airflow path as a dominant design variable, with Outdoor Air Curtain configurations showing significant potential in mild climates.

Nonetheless, the need for greater flexibility and new functionalities, such as thermal energy storage and more control over the temperature of the air from the cavity to the indoor environment, has driven the development of more advanced DSF versions, incorporating innovative strategies, materials and technologies. In fact, despite their potential, conventional DSFs also present several limitations that hinder their widespread applicability. A recurring challenge is the tendency of the cavity to overheat, particularly in summer and warm climates, which can increase cooling loads instead of reducing them if not properly managed [9,16]. This issue is exacerbated by the system's high dependence on ventilation strategies, shading devices, and external climatic conditions, which makes their performance highly variable [16]. Moreover, DSFs inherently lack significant thermal storage capacity, limiting their ability to shift or smooth temperature fluctuations throughout the day. To address these shortcomings, researchers have investigated the integration of Phase Change Materials (PCMs) into DSFs [17,18]. In this context, PCM-enhanced façades present a promising opportunity to enhance responsiveness by capturing and releasing thermal energy depending on environmental conditions [19,20]. Several experimental investigations have confirmed the potential of

PCM integration into glazing systems and ventilated façades to improve thermal buffering and reduce peak indoor temperatures without compromising daylighting or energy performance [21–23]. For instance, Goia et al. [24,25] demonstrated that a PCM-integrated double-glazed unit outperforms a conventional DGU (Double Glazing Unit) under higher levels of solar radiation, as the paraffin layer contributes both shading and thermal-buffering effects that improve thermal comfort and energy performance. Ziasistani et al. [26] demonstrated that incorporating PCMs into DSF systems enhances energy performance in different climates. Li et al. [27,28] tested the performance of encapsulated PCM blinds into DSF in Shanghai, and showed that PCM blades were found to absorb excess solar heat for about 5.9 h on average, the air-cavity stayed around 38–40 °C, avoiding overheating. Among the experimental studies in this area regarding double skin facades, De Gracia et al. [29] used two identical house-like test huts in Spain and fitted them with a south-facing ventilated double-skin façade (DSF) containing paraffin PCM panels in the cavity, concluding that adding the PCM-bearing ventilated façade made the building warmer in winter and cut heating loads, though forced ventilation. With the same test case De Gracia et al. [30] applied a strategy to charge the PCM at night (using cool outdoor air to solidify it) and discharge during peak daytime to supply cooling, demonstrating the feasibility of night-time cold storage. Grynning et al. [20] conducted large-scale testing of a PCM window under controlled cycling in a climate simulator, confirming latent heat activation under Nordic summer-like conditions. Similarly, Hu et al. [31] proposed a PCM-enhanced ventilated window through both simulation and full-scale testing, showing up to 62% summer cooling energy savings with optimized control strategies.

Despite numerous studies on DSF and PCM integration, experimental investigations under real outdoor conditions remain limited. Such investigations are essential to assess façade performance under dynamic boundary conditions and to derive normalized, physically grounded metrics. This is particularly relevant for multifunctional transparent components, whose performance results from the coupled interaction between solar radiation, cavity airflow, heat storage/release processes, and indoor–outdoor thermal boundary conditions. These interactions are difficult to capture through short-term tests, simplified laboratory procedures, or purely numerical approaches. However, standardized experimental protocols for multifunctional façades combining ventilation, solar control, and latent heat storage are still lacking. The simultaneous use of conventional static and more non-conventional performance metrics is crucial for fully understanding the complex and dynamic behaviour of such dynamic building envelope components. Full-scale experimental studies, such as Serra et al. [32] have demonstrated the adaptability of mechanically ventilated façades across seasons, while in-situ approaches [33] have proposed novel, low-cost methods to characterize glazing systems' U-values and g-values under real conditions. Previous efforts such as the ACTRESS module [34,35] and the broader ACTRESS and ADAPTIWALL projects [36] laid the foundation for experimental assessment of multifunctional façade systems integrating solar control, shading, and thermal storage. Similarly, Corgnati et al. [37] conducted long-term testing of an active transparent façade in an operational office environment, highlighting both the benefits and challenges of façade-integrated ventilation. These studies introduced important dynamic performance metrics, such as dynamic insulation efficiency, pre-heating efficiency, and thermal buffer efficiency, which are crucial in evaluating adaptive façades under real environmental variations.

1.2. Aims and outline of the research

This paper presents a prototype of an Heat Harvesting Window (HHW), integrating a fan-assisted narrow cavity ventilated triple glazing unit (TGU) with air to PCM heat exchanger (a-PCM HEX), placed at the cavity outlet. In a recent numerical study by the authors, the same façade system presented in this paper was assessed, evaluating its performance across different seasonal and ventilation scenarios by means of building performance simulations [38]. Results revealed the potential of the system to reduce ventilation-related heat losses and reducing heat gains by thermal buffering, particularly in winter, and helped to select appropriate climate specific PCM melting temperatures. However, while simulation provides valuable design insights, experimental validation remains essential to confirm performance under real boundary conditions. Therefore, full scale prototypes were developed within the research project, and one full-scale mock-up was installed on the South façade of an outdoor test facility. The novelty of this work is the full-scale experimental assessment of the HHW prototype under real outdoor boundary conditions. The main aim of this paper is to present the experimentally evaluation of the energy performance of such dynamic system in real climate (HDD (10 °C) 835 and CDD (18 °C) 360). The monitoring campaign spanned over 14 months (spanning heating, cooling and mid-season), during which the system was tested under various seasonal and operational conditions [39]. The experimental activity focused on evaluating both conventional static and dynamic Key Performance Indicators (KPIs) for the different components of the HHW (the ventilated cavity alone, the a-PCM HEX), and for the module as a whole. Different ventilation strategies and control configurations were explored to characterize the system's ability to adapt to external conditions and minimize energy losses, while maintaining high level of indoor thermal comfort with ventilation rates always enough to maintain a good level of indoor air quality. In the next section the HHW system and its subcomponents will be described, together with its operating principles. This is followed by a presentation of the experimental setup and the monitoring campaign for the energy performance assessment, together with the methods and the key performance indicators adopted. The results section presents the experimental performance characterization divided by seasons and operational modes of the innovative ventilated window. Finally, an energy balance is presented for the HHW in typical days (peak and average per season), so to allow a performance comparison with two triple glazing units, in terms of net transmission and ventilation heat transfer through whole building envelope component.

2. The heat harvesting window

2.1. HHW module objective & description

The Heat Harvesting Window system was in the framework of the European H2020 Open Innovation Test Bed iclimabuilt project [40]. It was designed to address key limitations in conventional transparent façade components and DSFs; which include reducing great energy losses from the building through the façade and insufficiency in providing enough natural ventilation for sustaining a healthy indoor environment. The developed HHW prototype combines ventilation adaptability, thermal buffering and latent heat storage capabilities within a modular window-integrated system. The prototype integrates a mechanically ventilated triple glazing unit and an air to phase change material heat exchanger, forming a compact and responsive Heat Harvesting Window (HHW) system. The complete HHW prototype is described in Fig. 1.

The HHW prototype was installed as a full-scale mock-up on the South façade of the TWINS (Testing Window Innovative Systems) outdoor test facility located on the rooftop of the Department of Energy of Politecnico di Torino, Italy (1.8 m × 4.5 m × 3 m height). The façade prototype measures 1.6 m in width and 2.5 m in height, which includes the transparent window module as well as the opaque lower and upper plenum zones with vents that serve as air inlets and outlets.

The transparent section spans 1.3 m × 1.7 m and is composed of (from outdoor to indoor):

- 6 mm external single-glazed pane;
- 30 mm ventilated cavity;

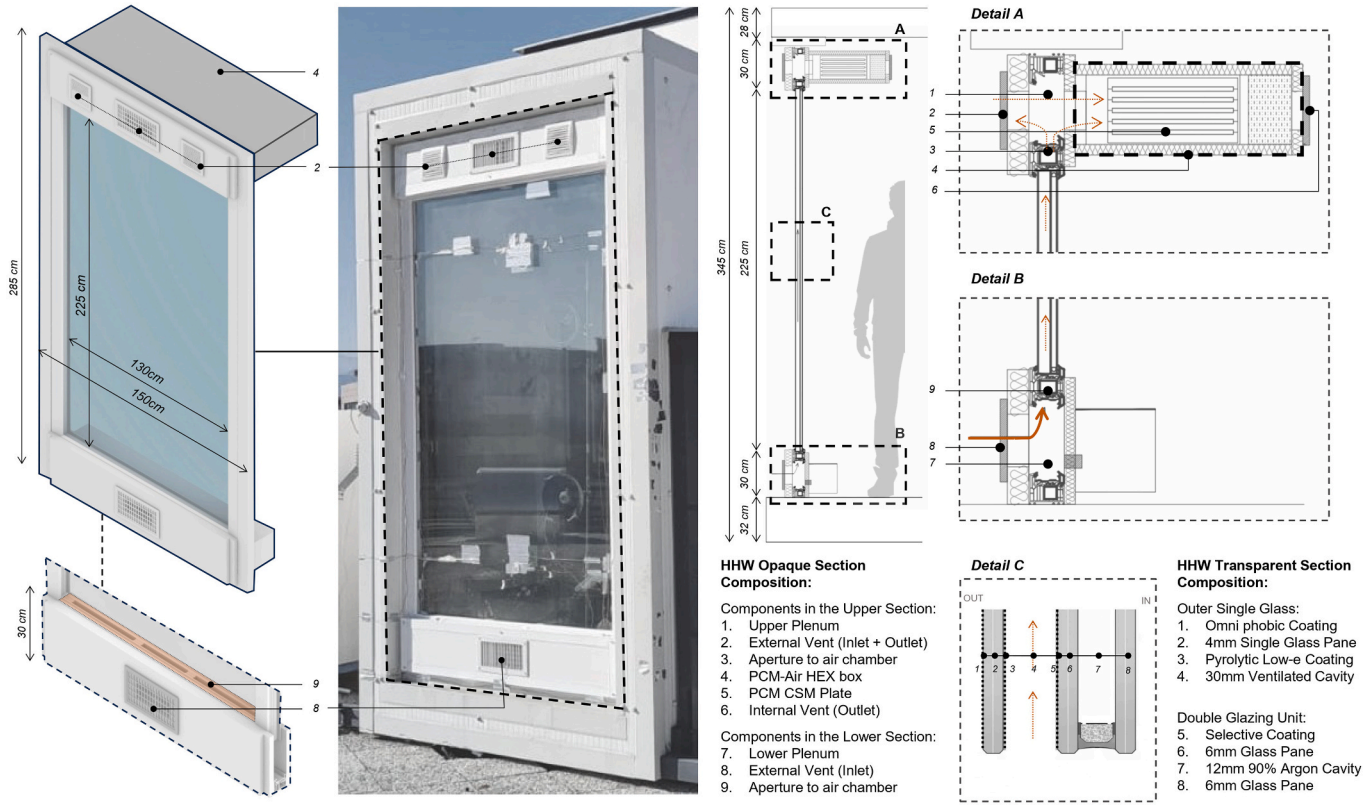


Fig. 1. Scheme of the HHW module and picture of the mock-up for the experimental investigation (left) and section view details (right).

- Double-glazing Unit filled with 90% Argon (6/12/6 mm), providing thermal insulation.

The system leverages advanced optical coatings to enhance its selective solar behaviour, including:

- An omniphobic self-cleaning coating on the first (external) glass pane surface facing outside.
- A pyrolytic low-emissivity coating on the first glass pane facing the cavity, allowing high visible and solar transmittance (so that enough solar radiation can reach the internal DGU) and infrared rejection;
- A selective solar-control coating on the second pane toward the cavity, promoting visible transmittance while reducing near infrared solar gains.

The optical properties of the glazing layers are summarized in Table 1.

The opaque section of HHW includes multiple components essential for managing the ventilation from the outdoor to the indoor environment, through the window outer cavity. Outdoor air enters through a lower vent into a plenum and is distributed into the cavity via three apertures (with a total area of 275 cm^2). The air introduced into the cavity is heated as it touches the glass surfaces absorbing solar radiation (total absorption $Abs_1 = 0.2541$ and $Abs_2 = 0.1646$), and propelled vertically through the cavity by dedicated axial fans into the upper opaque section of HHW or through buoyancy effect. At the top of the cavity, the air enters an upper plenum, from which it can be directed either to the a-PCM HEX or discharged outdoors, depending on the selected operating mode. Airflow rates are actively regulated through electronic controls, enabling seasonal and hourly adaptability.

Positioned above the transparent section, so that it could be hided within a false ceiling structure, the a-PCM HEX consists of independent heat exchanger units (2 in this case), each hosting five macro-encapsulated PCM plates from the SP-Line series by Rubitherm GmbH.

Table 1
HHW thermo-optical properties.

Parameter	Unit of Measure	Value
U-value	$W/(m^2K)$	1.13
SC	–	0.398
g-value	–	0.346
Rel. Ht Gain	W/m^2	257
Keff	W/(mK)	0.0804
Layer 1 Keff	W/(mK)	1
Gap 1 Keff	W/(mK)	0.0581
Layer 2 Keff	W/(mK)	1
Gap 2 Keff	W/(mK)	0.065
Layer 3 Keff	W/(mK)	1
τ_{vis}	–	0.503
Rfvis	–	0.1706
Rbvis	–	0.2021
τ_{sol}	–	0.19
Rfsol	–	0.3809
Rbsol	–	0.3429
Abs_1	–	0.2541
Abs_2	–	0.1646
Abs_3	–	0.0104

Each Compact Storage Module (CSM) is made of aluminium (450 × 300 × 15 mm) and contains 2 kg of salt hydrate PCM. The aluminium casing ensures effective thermal exchange, while anti-corrosive coatings protect against degradation. The a-PCM HEX recovers thermal energy through latent heat storage from either cavity air or outdoor air, depending on ventilation mode, while preserving the transparent area of the façade. The two a-PCM HEX contains PCM at different melting temperatures, the HEX1 contains has melting temperature of 21 °C, while HEX2 contains PCM with a melting point of 25 °C. The selection of the PCM transition temperatures was based on both previous numerical analyses and comfort-related operating criteria. A preliminary simulation study carried out for the Turin climate was used to compare

different PCM melting ranges and identify those providing the most favourable seasonal performance for the HHW system [38]. In addition, the selected transition temperatures were chosen to be close to the indoor comfort range and compatible with the expected thermal cycle of the façade cavity and supplied air. This allows the PCM to melt during periods of solar gains and higher cavity temperatures, and to solidify again when temperatures decrease, enabling repeated charge and discharge cycles under real outdoor conditions [41]. Table 2 summarizes PCM thermophysical characteristics from Rubitherm technical sheets.

The selected PCM melting temperatures (21 °C and 25 °C) were chosen based on typical climatic conditions in Turin and on the basis of previous numerical studies [38], ensuring the PCM effectively captures daytime heat during transitional seasons, while allowing night-time heat release to support passive heating. Nevertheless, the concept of the HHW is that the PCM melting temperatures can be optimized according to the local boundary (both outdoor climate and indoor heating and cooling set-point, where present). The use of two distinct melting temperatures enables direct comparison of system performance under varying conditions, assessing the influence of PCM phase-change temperature on overall effectiveness.

The HHW is engineered for continuous ventilation management (to ensure primary hygienic ventilation for the indoor space), and seasonal adaptability through three ventilation strategies (as depicted in Fig. 2):

a. Supply Air (SA): Outdoor air is drawn into the cavity, pre-heated by solar radiation, directed through the a-PCM HEX, which dampens temperature swings, and is then supplied to the indoor space. This mode maximizes solar heat recovery during heating periods, storing excess daytime energy in the PCM and releasing it at night to reduce ventilation heat losses.
b. Outdoor Air Curtain (OAC): Air flows from the outdoor environment to the cavity, and then it is returned to the outdoors, removing the absorbed solar radiation by the glazing layers and limiting secondary solar heat transfer to the indoor environment, when cooling needs are present. The a-PCM HEX can optionally process fresh air independently, exploiting day-night outdoor temperature swings to store heat into the PCM thus reducing ventilation heat gains.
c. Thermal Buffer (TB): Top and bottom vents are closed, minimizing transmission heat losses (or gains) through the glazing area. The a-PCM HEX can operate independently to ensure hygienic ventilation.

Fan speeds and vent positions are adjustable, offering fine-grained control over airflows and coupling strategies between the ventilated TGU (v-TGU) and the a-PCM HEX. Overall, the HHW innovative façade systems embodies a high level of modularity, thermal and ventilation management, thermal inertia, low maintenance, but also additional features such as local boundary conditions adaptability and low-intrusion integration, aiming to support future integration in Zero Emission and healthy Buildings.

Table 2
PCM thermophysical characteristics.

	PCM 21 °C	PCM 25 °C
Melting area [°C]	20–22	24–26
Congealing area [°C]	21–19	24–23
Heat storage capacity [kJ/kg]	170	180
Specific heat capacity [kJ/(kgK)]	2	2
Density solid [kg/l]	1,6	~1,6
Density liquid [kg/l]	1,5	~1,5
Volume expansion [%]	~ 6	~ 6
Heat conductivity [W/(mK)]	~ 0,5	~ 0,5

3. Experimental characterization of the HHW energy performance

The HHW module was installed as a full-scale mock-up on the South façade of the TWINS outdoor test facility located on the rooftop of the Department of Energy of Politecnico di Torino, Italy. The test cell provides an unobstructed Southern exposure and is raised 14 cm from the roof surface (average albedo 0.26), with internal dimensions of 3.6 m (depth), 2.5 m (height), and 1.6 m (width). The indoor air in the test cell was constantly kept at the desired set point value (20 °C in winter, 26 °C in summer, 23 °C in mid-season, with a tolerance of ±0.5°C both temporary and spatially) by means of a constant volume full air system. The opaque envelope (both vertical and horizontal) consists of double-steel polyurethane sandwich panels (120 mm, with a U-value of 0.25 W/(m^2K)), and the floor is additionally finished with linoleum.

The objective of the 14 months experimental campaign was two-fold:

- To characterize the thermophysical behaviour and thermal-energy performance of the individual subcomponents of the HHW façade system, namely the ventilated TGU and Air-to-Phase Change Material Heat Exchanger;
- To evaluate the overall performance of the HHW integrated façade system under dynamic boundary conditions, with particular focus on the seasonal adaptability of its operations to seasonal changes (for heating, cooling and mid- seasons).

Depending on the considered quantitative indicators adopted for the performance analysis (detailed in the next sections), the analysis was done either performed on specific design and/or average days, or on the basis of the whole set of experimental data referred to the considered seasonal period.

3.1. Measurement test rig and experimental plan

The measurement rig consisted of 100 sensors (among thermocouples, heat flow meters, pyranometers, air pressure probes, anemometers, wind direction and humidity sensors) and data loggers providing comprehensive data to characterize the outdoor environment in the test facility proximity, the indoor and surface conditions of the test cell, the ventilation exchange between the test cell and the outdoor environment, and the HHW module. The latter was equipped with 72 sensors for the measurements of the main thermo-physical quantities. The positions and the type of sensors are summarized in the Fig. 3 and can be divided into: Test Cell (Upper left Fig. 3) including outdoor climate station, v-TGU (Lower left Fig. 3) and a-PCM HEX (Right Fig. 3).

The measurement chain (each sensor connected to each data logger acquisition channel) was preliminary calibrated and/or verified in the laboratory, obtaining the following measurement accuracies: ±0.5 °C for thermocouples, ±3% and ± 5% for the heat flux meters (two types of heat flux meter were used), ±3% for the pyranometers, ±0.5% for differential pressure sensors (Δp) sensor reading +1 digit for a specific range of pressure specified by the manufacturer (±500 Pa).

The data acquisition from the whole sensor network is carried out by means of datalogger DataTaker DT85, with a scan rate of 5 min (measurements are done every 30 s and averaged on 5 min), and then averaged with a 15 mins and hourly basis. The airflow through the v-TGU was characterized offline in order to relate fan rotational speeds (% of fan power), anemometric measurements within the ventilated cavity and at the indoor vents (between a-PCM HEX vent and indoor environment, at the HVAC return vent and within the return cylindrical channel of the HVAC), and continuous airflow measurements carried out by means of Pitot tube and differential pressure measurements.

The inlet lower vent was divided into nine subsections, and the local velocity was measured at the centre of each subsection. The volumetric flow rate was calculated as:

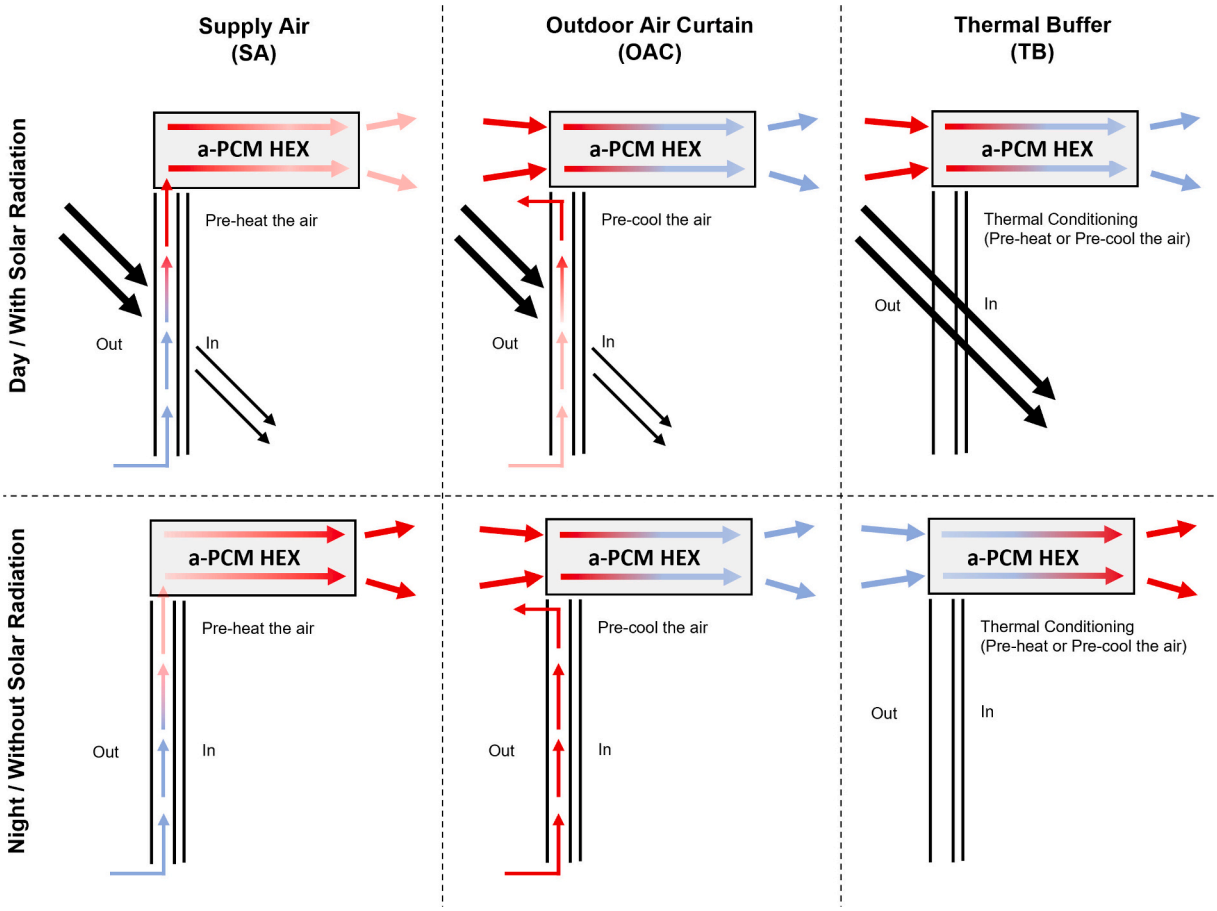


Fig. 2. HHW Ventilation modes.

$$V_{low,vent} = \sum_{i=1}^{n} v_i \frac{A_i}{A_{tot}} \quad (1)$$

Assuming continuity, the average cavity velocity was obtained as:

$$v_{cav} = \frac{V_{low,vent}}{A_{cav}} \quad (2)$$

where $A_{cav}$is the cavity cross-sectional area. Since the online hot-wire anemometers provide punctual measurements potentially affected by obstructions inside the cavity, a linear correlation was established between offline measurements and online readings. This correction allows continuous estimation of the cavity airflow rate during operation. A similar procedure was applied to the outlets of HEX1 and HEX2 in Supply Air (SA) mode. Due to the smaller outlet section, the area was divided into two subsections (upper and lower), with velocity measured at the centre of each. Finally, a fan power matrix was developed by varying upper and lower fan speeds from 0 to 100% to fully characterize the airflow modulation capability of the system (Table 3). Reflective aluminium external shields were used in order to minimize the disturbances of the solar radiation over the heat fluxes and temperature sensors.

The whole monitoring plan was designed to ensure a comprehensive performance characterization of the different sub-components (v-TGU and a-PCM HEX) and of the HHW module as a whole, in all the operating modes (SA, OAC and TB) across heating, cooling and mid-season conditions. Table 4 reports only the validated and most representative periods selected for the performance assessment, corresponding to the seasonal and operational cases considered most relevant to the objectives of the study. The experimental campaign aimed to evaluate the thermo-fluid dynamic behaviour of the system under a wide range of boundary conditions. To this end, different fan speeds and mass flow rates were intentionally applied across seasons. The objective was not to assess indoor air quality compliance, but to investigate performance limits and responsiveness of the façade system. Therefore, relatively high air change rates were explored to analyse the sensitivity of both the ventilated cavity and the a-PCM HEX to airflow intensity. As with the variation in PCM melting temperatures, airflow modulation enabled identification of optimal operating regimes.

3.2. *Method and parameters adopted for the performance analysis*

Given that the HHW system consists of two dynamic components, the v-TGU and the a-PCM HEXs, operating with multiple ventilation strategies, its performance is assessed through a combination of standardized and non-standardized performance metrics. The standardized metrics are used to benchmark the performance of the HHW components against conventional glazing façade technologies, in accordance with recognized building standards. In contrast, the non-standardized metrics are introduced to capture the innovative and dynamic behaviour of the system. These indicators are either adapted from relevant literature or developed specifically to reflect the unique operational characteristics of the HHW façade module. Equally important is the methodology adopted for data post-processing and visualization, which plays a critical role in interpreting performance outcomes. Fig. 4 summarize the methodology developed. The diagram is organized according to the system hierarchy and the type of KPI considered. The pink blocks refer to the whole HHW component, while the blue and green blocks identify the two main subcomponents, the v-TGU and the a-PCM HEX. Moving from top to bottom, the figure reports the different groups of performance indicators, from component-level characterization to system-level energy balance and

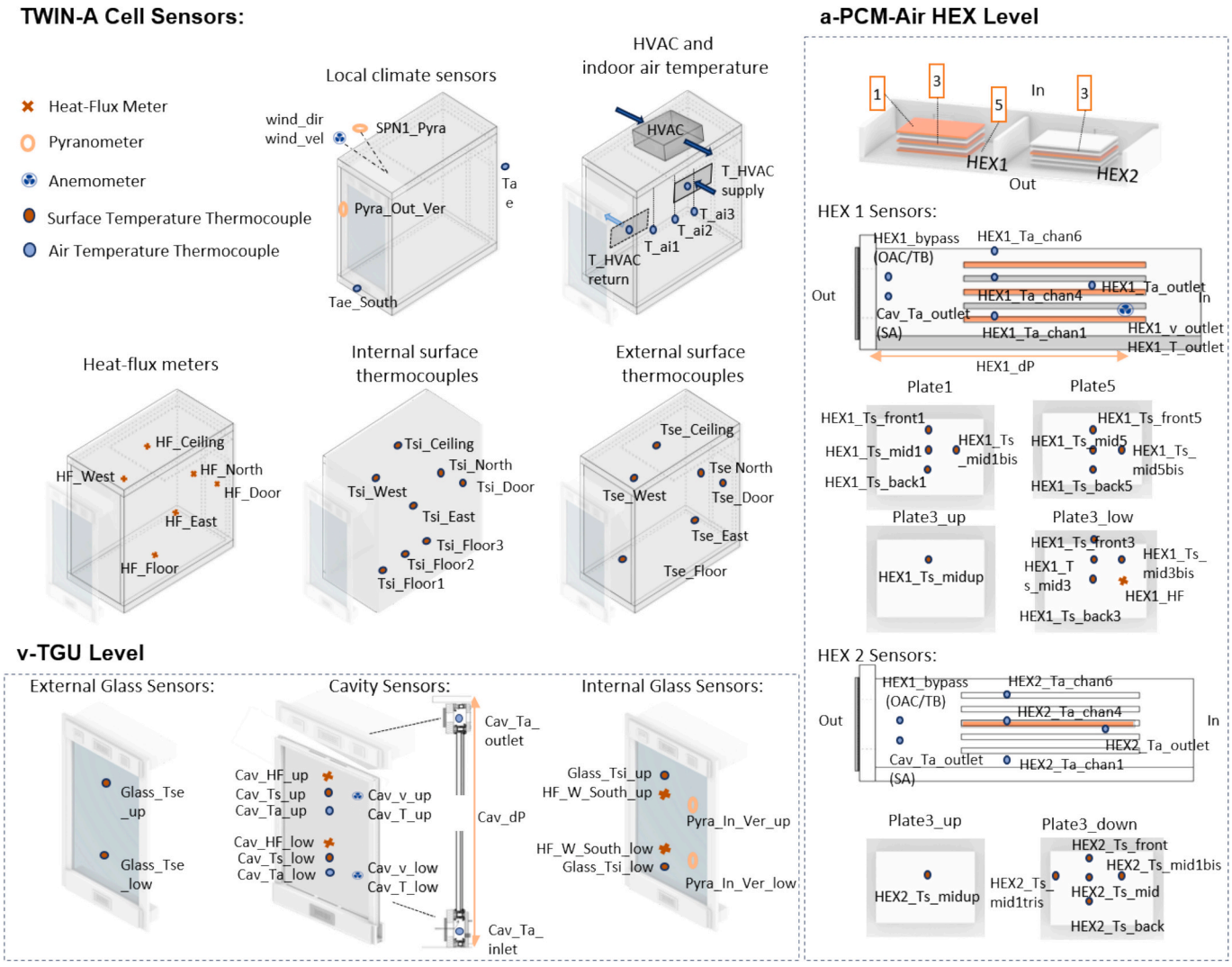


Fig. 3. Experimental apparatus: TWIN cell (Upper left), Ventilated TGU (v-TGU) level (Lower left), Heat exchanger 1 and Heat exchanger 2 (HEX1 and HEX2) (Right).

Table 3
Airflow characterization matrix.

%fan_LowVent	%fan_HighVent				
	0%	10%	30%	50%	100%
0%	0,00	3,62	5,41	7,23	9,39
10%	0,00	3,78	5,20	7,06	9,41
30%	0,00	3,74	5,20	6,92	9,26
50%	0,00	3,57	5,22	6,71	8,85
100%	0,00	3,43	5,26	6,81	8,74

dynamic efficiency metrics. The colour and position of each KPI indicate whether it refers to the v-TGU, the a-PCM HEX, or to the integrated HHW system as a whole. For efficiency metrics, cumulative frequency distributions are used to quantify the proportion of time specific performance levels are achieved, providing insight into system consistency and reliability. In contrast, energy balance analysis and comparison with static components are based on representative "typical days," reflecting both average and peak seasonal conditions. These reference days are defined according to the Italian standard UNI 10349–1 [42], which provide monthly climatic data on average and peak temperatures as well as solar radiation levels, with the national Italian territory.

3.2.1. *Thermal conductance and thermal transmittance*

The thermal transmittance (U-value), quantifies the steady-state heat transfer rate through a building element per unit area per unit temperature difference between the indoor and outdoor environments.

3.2.1.1. Thermal conductance Λ. The thermal conductance, was determined experimentally from the relationship between measured heat flux density and the temperature difference across the façade surfaces. Under quasi steady-state conditions:

$$q = \Lambda \cdot (T_{si} - T_{se}) \quad (3)$$

where:

- q is the measured specific heat flux density [W/m^2],
- T_{si} and T_{se} are the indoor- and outdoor-facing surface temperatures [°C],
- Λ is the thermal conductance of the component [W/(m^2·K)].

Λ was obtained using Ordinary Least Squares (OLS) regression, with the slope of the linear correlation between heat flux and surface temperature difference representing the conductance [37]. To reduce transient effects and solar influence, the dataset was filtered by considering only nighttime measurements, excluding data within 3 h

Table 4
Representative monitoring periods selected for the quantitative performance analysis.

Season	Strategy	Measurement period [days]	Temperature Setpoint [°C]	Fan Speed [%]		Flow Rate to indoor environment [m³/h per m of facade]	ACH to indoor environment [vol/h]
				Bottom fan	Top fan (HEX)		
Winter	SA	35	20	30%	10%	99.31	7.48
		5	20	30%	50% – Day 10% - Night	184.09 – Day 99.31 - Night	13.84 – Day 7.48 - Night
	TB	48	20	–	10%	96.11	7.24
Mid-season	SA	16	23	10%	30%	138.26	10.82
		8	23	30%	50% – Day 10% - Night	184.09 – Day 99.31 - Night	13.84 – Day 7.48 - Night
	TB	10	23	–	10%	96.11	7.24
Summer	OAC	56	26	100%	100%	232.31	17.48
	OAC/ TB every 30 mins	6	26	100% / 0%	0% / 100%	0 / 249.56	0 / 17.48

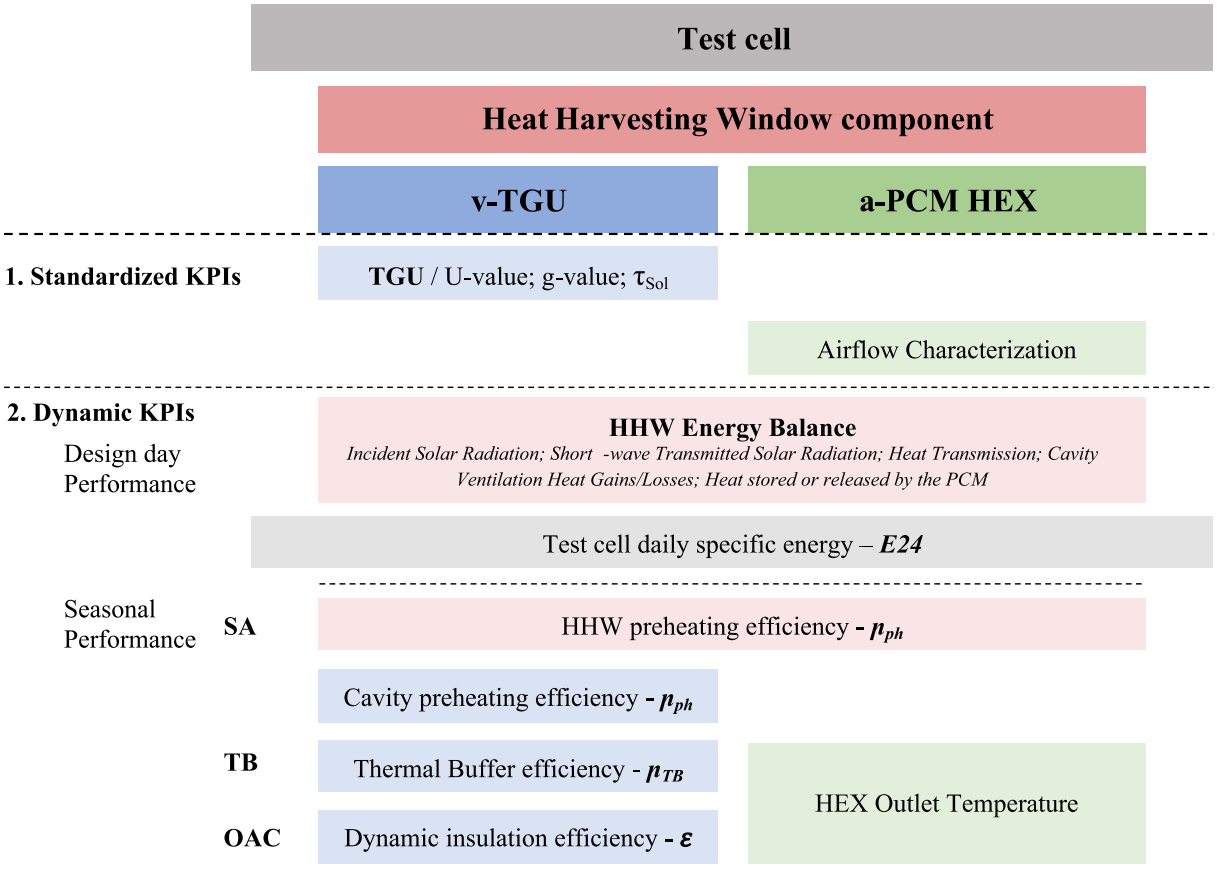


Fig. 4. Key Performance Indicators of the HHW experimental characterization

after sunset and discarding periods with unstable boundary conditions. This procedure minimized distortions due to solar gains and thermal inertia.

3.2.1.2. Thermal transmittance (U value). Two thermal transmittances were calculated: a nominal U-value and an effective U* [38].

Regulatory U-values refer to standardized boundary conditions. According to EN ISO 6946 (2007), the internal and external surface resistances for vertical elements are:

$R_{si} = 0.129\,\mathrm{m^2K/W}$

$R_{se} = 0.04\,\mathrm{m^2K/W}$

Nominal thermal transmittance (U-value).

The nominal U-value was calculated from the measured conductance Λ by adding the standardized surface resistances:

$$U - value = \frac{1}{R_{si} + \frac{1}{\Lambda} + R_{se}} \quad (4)$$

This formulation enables direct comparison with regulatory requirements.

Effective thermal transmittance (U*).

The effective thermal transmittance was determined directly from measured data, using indoor and outdoor air temperatures:

$$q = U^{*} \cdot (T_{in} - T_{out}) \tag{5}$$

where:

- $T_{in}$and $T_{out}$are the indoor and outdoor air temperatures [°C].

U* was obtained via OLS regression of heat flux density against air temperature difference. The slope represents U*, reflecting the in-situ thermal performance under real boundary conditions.

3.2.2. Experimental Solar Transmittance – τ_{sol} [–]

The solar transmittance τ_{sol} represents the fraction of incident solar radiation transmitted through the glazing. It was evaluated using measurements from external and internal pyranometers installed on the HHW façade.

The parameter is defined as:

$$\tau_{sol} = \int \frac{I_{v,in}}{I_{v,out}} \tag{6}$$

Where:

- $I_{v,in}$ is the transmitted solar radiation measured by the internal pyranometers [W/m^2].
- $I_{v,out}$ is the total incident solar radiation measured by the external pyranometer [W/m^2].

Since glazing transmittance depends on the angle of incidence (AOI, θ) due to reflection and absorption effects, instantaneous $\tau_{s_o|}$ values were associated with their corresponding AOI and grouped into angular bins. $\tau_{s_o|}$ was plotted a function of AOI. The dataset was filtered by:

- considering only daytime data with non-zero irradiance,
- excluding very low irradiance levels (near sunrise and sunset),
- discarding values outside the physical range $0 \leq \tau_{sol} \leq 1$.
- For each analysed period, two representative values are reported:
- the period-averaged solar transmittance, computed over the filtered daytime dataset.
- the near-normal solar transmittance, corresponding to the AOI closest to 0°.

3.2.3. Experimental total solar energy transmittance (SHGC or g-value)

The total solar energy transmittance (SHGC or g-value) quantifies the fraction of incident solar energy contributing to indoor heat gain. It includes the directly transmitted solar radiation and the secondary heat transfer from the glazing toward the indoor environment by convection and long-wave radiation.

Under in-situ conditions, direct calorimetric measurement is not feasible. Therefore, an effective g-value (g*) was determined using a non-calorimetric approach consistent with [35] and with the methodology described by Goia & Serra [33].

The daily g-value was computed as:

$$g - value = \frac{E_{in}}{H_{v,out}} \tag{7}$$

Where:

- $H_{v,out}$ is the total solar energy incident on the façade, obtained by integrating the external pyranometer signal over time [Wh/m^2],
- E_{in} is the total daily solar energy gain to the indoor environment [Wh/m^2],

The incident solar energy was calculated as:

$$H_{v,out} = \int_{24h} I_{v,out}(t)\, dt \tag{8}$$

where $I_{v,out}(t)$is the measured external vertical solar irradiance.

The total energy entering indoors is composed of:

1. Direct solar transmission

$$H_{in} = \int_{24h} I_{v,in}(t)\, dt \tag{9}$$

2. Secondary heat transfer from the glazing

$$Q_{II,in} = \int_{24h} \dot{Q}_{II,in}(t)\, dt \tag{10}$$

Thus:

$$E_{in} = H_{in} + Q_{II,in} \tag{11}$$

The heat flux meters installed on the internal glass surface measure the total surface heat flux:

$$\dot{Q}_{surf}(t)$$

This includes:

$$\dot{Q}_{surf} = \dot{Q}_{\Delta T} + \dot{Q}_{II,in} \tag{12}$$

where:

- $\dot{Q}_{\Delta T}$is the heat transfer due to the indoor-outdoor temperature difference,
- $\dot{Q}_{II,in}$is the secondary solar heat gain.

To isolate the secondary contribution, the temperature-driven heat flux was estimated using the previously determined effective thermal transmittance U^{*}:

$$\dot{Q}_{\Delta T}(t) = U^{*} \cdot (T_{out}(t) - T_{in}(t)) \tag{13}$$

Therefore, the secondary heat flux becomes:

$$\dot{Q}_{II,in}(t) = \dot{Q}_{surf}(t) - U^{*} \cdot (T_{out}(t) - T_{in}(t)) \tag{14}$$

Integrating over 24 h:

$$Q_{II,in} = \int_{24h} \dot{Q}_{surf}(t)\, dt - \int_{24h} U^{*} (T_{out}(t) - T_{in}(t))\, dt \tag{15}$$

Substituting all terms, the effective total solar energy transmittance becomes:

$$g - value^{*} = \frac{\int_{24h} I_{v,in}(t)\, dt + \left[\int_{24h} \dot{Q}_{surf}(t)\, dt - \int_{24h} U^{*} (T_{out}(t) - T_{in}(t))\, dt\right]}{\int_{24h} I(t)\, dt} \tag{16}$$

All quantities I_{in}, I, $\dot{Q}_{surf}$, T_{out}, and T_{in}were directly measured during the monitoring campaign, while $U^{*}$was experimentally determined as described in Section 3.2.1.

As with τ_{sol}, this metric represents an effective value under real operating conditions and cannot be directly compared to standardized values reported by manufacturers, which are often based on steady-state laboratory tests.

3.2.4. Cavity pre-heating efficiency – η_{PH} [–]

The energy performance of the HHW, when operating in Supply Air (SA) mode, was assessed by means of the so-called pre-heating efficiency, η_{PH} [43], which quantifies the system's ability to increase the temperature of incoming outdoor air by exploiting solar and thermal gains within the cavity.

$$\eta_{PH} = \frac{T_{outlet} - T_{inlet}}{T_{in} - T_{out}} \quad (17)$$

Where:

- T_{outlet} is the air temperature supplied indoors(°C)
- T_{inlet} is the inlet air temperature which correspond to the outdoor air temperature T_{out} (°C)
- T_{out} is the outdoor air temperature (°C)
- T_{in} is the indoor air temperature (°C)

The definition of the outlet temperature determines the system boundary considered. The efficiency may refer to the entire HHW system, when T_{outlet} is measured downstream of the air to PCM heat exchanger ($T_{outlet} = T_{hex,outlet}$) or the glazed cavity only, when the temperature is measured at the cavity exit ($T_{outlet} = T_{cav,outlet}$), upstream of the PCM unit. Both configurations are analysed in the Results section to evaluate the impact of PCM integration on pre-heating performance.

The interpretation of η_{PH} is as follows:

- $\eta_{PH} < 0$, the outlet air temperature, T_{outlet}, is lower than the indoor temperature, T_{in}, and, hence, there is no energy recovery. In this condition, the only positive effect of the ventilated facade is the dynamic thermal insulation which is assured by the air flow rate;
- $0 < \eta_{PH} < 1$, the air is pre-heated but remains below indoor temperature, requiring additional heating before supply.
- $\eta_{PH} = 1$, the façade fully pre-heats the ventilation air, theoretically eliminating ventilation heat losses.
- $\eta_{PH} > 1$, the outlet air exceeds indoor temperature, fully compensating ventilation losses and partially offsetting other thermal losses.

This parameter is particularly relevant during winter and mid-season operation in SA mode, when solar gains can be exploited to pre-heat the ventilation air flowing through the HHW [32].

3.2.5. Cavity thermal buffer efficiency – η_{TB} [−]

The energy performance assessment of the HHW, when operating in Thermal Buffer (TB) mode (e.g. closed air cavity), can be carried out by introducing the efficiency η_{TB}, which is defined according as:

$$\eta_{TB} = \frac{T_{out} - T_{cav}}{T_{out} - T_{in}} \quad (18)$$

Where:

- T_{cav} is the cavity air temperature (°C)
- T_{out} is the outdoor air temperature (°C)
- $T_{in}$is the indoor air temperature (°C)

The interpretation of η_{TB} is as follows:

- when $\eta_{TB} < 0$, cavity air temperature (T_{cav}) is lower than outdoor temperature (T_{out}), increasing heat losses compared to the absence of a cavity.
- when $\eta_{TB} = 0$, cavity air temperature (T_{cav}) is equal to the outdoor temperature (T_{out}), heat losses are equivalent to a façade without cavity.
- when $0 < \eta_{TB} < 1$, cavity air temperature (T_{cav}) is higher than the outdoor temperature (T_{out}), and therefore the cavity reduces transmission heat losses.
- when $\eta_{TB} = 1$, cavity air temperature (T_{cav}) is equal to the indoor air temperature(T_{in}), and therefore no heat loss occurs from the inside to the cavity;
- when $\eta_{TB} > 1$, cavity air temperature (T_{cav}) is higher than the indoor air temperature (T_{in}), and therefore heat gain occurs from the cavity toward the indoor environment.

3.2.6. Cavity Dynamic insulation efficiency – ε [−]

The dynamic insulation efficiency [32], evaluates the capability of the HHW, operating in Outdoor Air Curtain (OAC) mode, to reduce heat flux entering the indoor environment through cavity ventilation:

$$\varepsilon = \frac{\dot{Q}_{cav}}{\dot{Q}_{out}} \; [-] \quad (19)$$

$$\varepsilon = \frac{\dot{m}_v \bullet c_{p,air} \bullet \left(T_{cav,outlet} - T_{cav,inlet}\right)}{\overline{q}_i \bullet A_{glass} + \overline{q}_{sw} \bullet A_{glass} + \dot{m}_v \bullet c_{p,air} \bullet \left(T_{cav,outlet} - T_{cav,inlet}\right)} \quad (20)$$

Where:

- $\dot{m}_v$ is the the air mass flow rate in the cavity.
- $(T_{cav,outlet} - T_{cav,inlet})$ is the temperature difference between the outlet and inlet of the cavity
- A_{glass} is the area of the glass
- $\overline{q}_i$ is the average specific heat flux measured on the inner glass pane
- $\overline{q}_{sw}$ is the specific heat flux entering due to the solar radiation (short wave radiation) transmitted through the façade measured by the two inner pyranometers.

The numerator represents the thermal power removed by ventilation, while the denominator represents the total heat flux directed toward the indoor side. To better interpret the physical meaning of ε, the possible ranges of values can be described as follows:

- $\varepsilon < 0$: The airflow increases the heat transfer toward the indoor side (e.g., when the cavity air temperature rise enhances inward heat flux). In this case, the dynamic insulation effect is detrimental under the given conditions.
- $\varepsilon = 0$: The ventilation airflow does not remove any portion of the incoming heat flux. The façade behaves as a static system.
- $0 < \varepsilon < 1$: The cavity ventilation removes a fraction of the entering heat flux. The façade operates effectively as a dynamic insulation system, partially reducing solar and conductive heat gains.
- $\varepsilon = 1$: The ventilation airflow removes all the incoming heat flux theoretically reaching the indoor environment. Under this ideal condition, the dynamic insulation fully compensates the entering heat gains.
- $\varepsilon > 1$: The airflow removes more heat than the calculated inward flux, indicating additional heat extraction from the façade under transient or high-ventilation conditions.

3.3. Energy balance of the HHW

To evaluate the global performance of the HHW façade system, an analysis of the energy flows through the HHW was conducted for representative seasonal days in accordance with the UNI 10349 [36]. This energy balance refers only to the HHW and not to the indoor environment. Each heat-transfer contribution was initially calculated as an instantaneous thermal power rate, denoted by $\dot{Q}$ and expressed in W. The corresponding daily energy contribution, denoted by Q, was then obtained by integrating the thermal power rate over the selected 24-h period. The heat transferred from the HHW toward the outdoor environment is considered negative, while heat flows toward the indoor environment are considered positive. Five key contributions were defined, shown graphically in the example in Fig. 5:

1. Incident Solar Radiation: measured by the external pyranometer, multiplied by the glazing area, as measured by external pyranometers.

$$\dot{Q}_{I,ver}^{HHW} = I_{v,out} \bullet A_{glass} \quad (21)$$

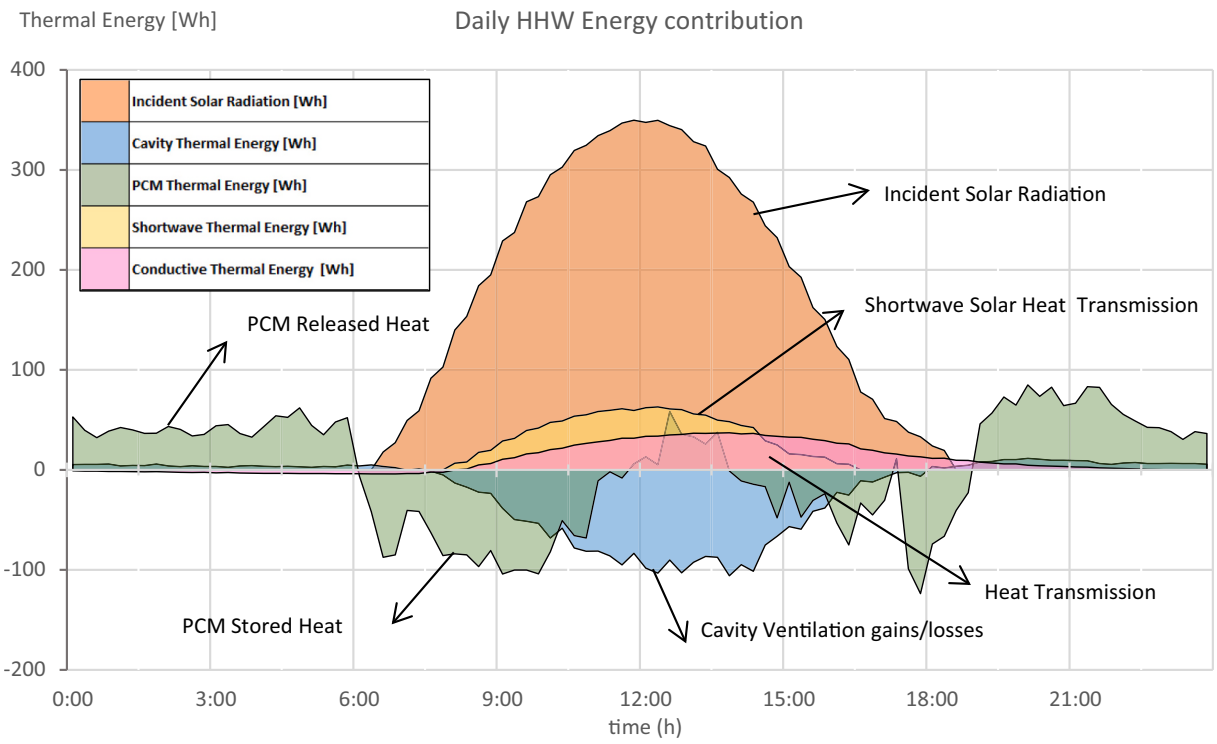


Fig. 5. Daily HHW energy contributions example (heat transferred toward the outdoor environment is considered negative, while heat gains toward the indoor environment are considered positive).

2. Shortwave Transmitted Solar Radiation, as measured by the internal pyranometers and multiplied by the glazing area.

$$\dot{Q}_{sw}^{HHW} = I_{v,in} \bullet A_{glass} \tag{22}$$

3. Heat Transmission: is the convective and radiative heat transfer through the glazing, as measured by heat flux sensors on the internal glass pane (including long-wave solar radiation secondary heat flux). This quota refers only to the glass heat transmission and it does not take into account thermal bridges.
4. Cavity Ventilation Heat Gains/Losses: it represents the temperature difference between the outlet air from the cavity and the inlet air entering it. Positive values indicate that thermal energy harvested in the cavity (pre-heated) through the exploitation of solar energy, is entering the indoor environment (e.g. in SA mode). Whereas negative representation conveys the expulsion of this energy toward the outdoors, avoiding it to enter in the indoor environment (e.g. in OAC mode).

$$\dot{Q}_{cav}^{HHW} = \dot{m}_v \bullet c_{p,air} \bullet \left(T_{cav,outlet} - T_{cav,inlet}\right) \tag{23}$$

Heat stored or released by the PCM (positive when discharging, negative when charging): This represents the temperature difference between outlet air form the HEX, and air entering it (either from cavity or from outdoors). Positive values occur when it is discharging and negative when it is charging

$$\dot{Q}_{pcm}^{HHW} = \dot{m}_v \bullet c_{p,air} \bullet \left(T_{hex,outlet} - T_{hex,inlet}\right) \tag{24}$$

Along with heat flows, temperatures are also represented in the same graph in the Results and Discussion section (not shown in Fig. 4), so to understand the physical mechanisms occurring at each component of HHW, including outdoor and indoor air temperatures, cavity outlet temperature, and HEX1 and HEX2 outlet temperatures. It should be noted that the present energy balance accounts only for the thermal energy flows exchanged through the HHW façade module. The electrical energy consumption of the fan was not included, since the aim of this analysis was to isolate the thermal contribution of the ventilated cavity and of the air to PCM heat exchanger under measured boundary conditions, rather than assessing the impact on building final energy uses. In the tested prototype, each axial fan had a nominal electrical power of 2.88–3 W, with a maximum of two fans operating simultaneously. Assuming continuous operation over one day, the maximum fan electricity consumption is 144 Wh day^{-1}, corresponding to 49.2 Wh m^{-2} day^{-1} when normalized over the glazed area. As an example, for the representative winter Thermal Buffer day discussed in Section 4.3.2 and shown in Fig. 12, this value corresponds to 5.5% of the positive heat gains and 3.0% of the heat losses reported in Table A1. For the representative summer Outdoor Air Curtain day shown in Fig. 14, it corresponds to 2.5% of the positive heat gains and 5.8% of the heat losses reported in Table A1. Therefore, although fan electricity consumption should be included in a whole-system net operational energy assessment, its contribution is limited with respect to the component-level thermal balance analysed here.

3.4. Comparative performance assessment of HHW and TGU

To assess the impact of the HHW on indoor conditions, the net daily energy transferred from the façade to the indoor environment was evaluated and compared with two TGUs. Compared to the daily energy balance of the previous paragraph, only the energy contributions affecting the indoor environment were considered and integrated over 24 h. The following assumptions were adopted for the comparative assessment:

- Indoor air temperature was maintained at the seasonal set-points defined in the experimental campaign (20 °C winter, 23 °C mid-season, 26 °C summer).
- For all systems, the in field measured airflow rates corresponding to each operating mode were used.

- For the reference TGU systems, ventilation was assumed as direct outdoor air supply to the indoor environment, without heat recovery, using the same airflow rate adopted for the corresponding HHW scenario to ensure comparability.
- Optical and thermal properties of the TGU were obtained from WINDOW simulations.

Two reference TGU configurations were considered:

1. "TGU" with thermal and optical properties equivalent to the glazing of the HHW.
2. "TGU-Benchmark" with U-value = 0.7 W/(m^{2}K) (optical properties equal to HHW), representative of commonly available commercial triple-glazed units.

The total energy flow passing through the HHW and TGU was decomposed into four main components, as follows:

- Shortwave solar gains: for HHW, TGU and TGU-benchmark the shortwave radiation is calculated in the same way. It's product of the experimental τ_{sol} (each timestep) and the total incident solar radiation on the façade. This ensures that differences in shortwave gains are not driven by angular transmittance discrepancies but solely by dynamic effects such as ventilation, longwave exchange, and thermal transmission.

$$\dot{Q}_{sw}^{HHW} = \dot{Q}_{sw}^{TGU} = \dot{Q}_{sw}^{TGUbencmark} = \tau_{sol} \bullet I_{v,out} \bullet A_{glass} \quad (25)$$

- Longwave or secondary solar gains: difference between the total solar end energy transmittance (g-value) and the solar transmittance (τ_{sol}). This difference was then multiplied by the incident vertical solar radiation, capturing the portion of energy re-emitted and convectively transferred indoors following absorption by the façade.

$$\dot{Q}_{lw}^{HHW} = \left(g - value^{HHW} \quad \tau_{sol}\right) \cdot I_{v,out} \bullet A_{glass} \quad (26)$$

$$\dot{Q}_{lw}^{TGU} = \dot{Q}_{lw}^{TGUbenchmark} = \left(g - value^{TGU} \quad \tau_{sol}\right) \cdot I_{v,out} \bullet A_{glass} \quad (27)$$

- Transmission energy losses or gains were calculated multiplying the thermal transmittance (U-value) by the measured temperature difference between indoor and outdoor air. Values recorded through the heat flux meters positioned inside the internal pane are considered for the conductive heat transfer through HHW.

$$\dot{Q}_{tr}^{TGU} = A_{glass} \bullet U_{TGU} \cdot (T_{in} - T_{out}) \quad (28)$$

$$\dot{Q}_{tr}^{TGUbenchmark} = A_{glass} \bullet U_{TGUbenchmark} \cdot (T_{in} - T_{out}) \quad (29)$$

$$\dot{Q}_{tr}^{HHW} = A_{glass} \bullet q_{glass}(t) \quad (30)$$

- Ventilation energy contribution was estimated based on measured airflow rates within the HHW cavity, multiplied by specific heat capacity of the air and its density at the specific air temperature, and by the temperature difference air supplied from the a-PCM HEX to the room and the indoor air (considering that the ventilation is directed from outdoor to indoor, without any heat recovery).

$$\dot{Q}_{vent}^{TGU} = \dot{Q}_{vent}^{TGUbenchmark} = \dot{m}_v \bullet c_{p,air}(T_{out} - T_{in}) \quad (31)$$

$$\dot{Q}_{vent}^{HHW} = \dot{m}_v \bullet c_{p,air}\left(T_{hex,outlet} - T_{in}\right) \quad (32)$$

This comparative methodology reflects not only steady-state performance metrics but also dynamic and latent contributions that become relevant in adaptive façade systems. All contributions were expressed in terms of daily energy [Wh/m^2 of facade] and integrated over a full day. The analysis was repeated for different representative climatic days, allowing for a comparison across distinct boundary conditions.

4. Results and discussion

The objective of the experimental campaign is to comprehensively evaluate the thermal and energy performance of the HHW façade system under representative operational conditions for winter, mid-season, and summer scenarios. To achieve this objective, a range of distinct operational configurations and ventilation strategies were subjected to the assessment, using both conventional and dynamic key performance indicators (KPIs). Conventional metrics, including U-value, g-value, and solar transmittance (τ_{sol}) facilitated direct comparison of the HHW performance with that of traditional façade technologies. On the other hand, the employment of dynamic metrics, including thermal buffer efficiency, pre-heating efficiencies, dynamic insulation efficiency, and overall energy balance facilitated the effective quantification of the adaptive and responsive behaviour inherent to the HHW system. Given the variability of the applied ventilation strategies in relation to seasonal conditions, the Results and Discussion sections are structured on a season-by-season basis, with each season divided according to the specific ventilation strategy implemented. For clarity and precision in the analysis, representative experimental periods from the experimental campaign will be presented in the next section.

4.1. Conventional key performance indicators

The conventional performance metrics summarized in Table 5 describe the behaviour of the v-TGU under different seasonal and operational modes. To enable comparison with results obtained under static conditions, steady-state KPIs were calculated using the WINDOW software [44] in accordance with the CEN standard. These values, referred to as "simulated TGU properties," represent the HHW operating as a conventional triple glazing unit (TGU) without airflow. When comparing simulated and experimental results, the influence of ventilation becomes evident. The measured U-values increase from approximately 1.04 W/(m^{2}K) in TB mode to 1.91 W/(m^{2}K) in SA mode, reflecting the enhanced convective heat transfer induced by cavity airflow. Moreover, the forced airflow decreases the effective thermal resistance of the cavity, further increasing the overall thermal transmittance of the system. In contrast, in TB mode the cavity is sealed and no ventilation occurs. Under these conditions, the system closely resembles a static triple glazing unit, yielding U-values near the simulated reference value of 1.13 W/(m^{2}K) obtained with WINDOW.

The average solar transmittance (τ_{sol}), showed in Fig. 6 is approximately 0.15 across tested incidence angles, after filtering unrealistic values and low irradiance data to ensure reliability. The experimental g-values showed in Fig. 6, range from 0.14 (winter SA mode) to 0.23 (mid-season TB mode), all significantly lower than the simulated steady-state value of 0.346 for a comparable TGU. This discrepancy primarily arises from the dynamic behaviour of the ventilated HHW system that static simulation tools cannot fully capture. Moreover, the peak solar altitude varies significantly across the analysed periods, ranging from approximately 30° in winter to over 60° in mid-season and summer, resulting in different angles of incidence on the façade. In SA mode, cavity ventilation removes part of the absorbed solar energy through the airflow, reducing the net solar gains entering the indoor space. The steady-state simulation, which assumes no airflow, therefore overestimates solar transmission. In TB mode, the sealed cavity acts as a thermal buffer, absorbing and temporarily storing solar energy, part of which is re-radiated outward or dissipated toward the exterior, further lowering the effective g-value. In Outdoor Air Curtain (OAC) mode, continuous airflow enhances convective heat removal within the cavity, further decreasing solar heat transmission to the interior. The differences between simulated static metrics and measured ones, and the range of

Table 5
Conventional performance metrics * the U-value measurement is highly affected by the ventilation of the air cavity, therefore not relevant.

Season	Window Operation	Cavity Mass Flow Rate [m^3/h per m of Facade]	U-value [W/(m^2K)]		Period Peak Solar Altitude [°]	τ_{sol} [−]		g-value [−]	
			Normalized	Experimental		average	at AOI closest to 0°	range	average
Winter	SA	99.31	1.66	1.91	29.97	**0.14**		0.03–0.2	**0.14**
	TB	–	1.38	1.18	56.27	**0.13**		0.03–0.26	**0.2**
Mid-Season	SA	138.26	1.65	1.62	65.27	**0.07**	**0.194**	0.01–0.19	**0.12**
	TB	–	1.1	1.04	36.79	**0.16**		0.18–0.27	**0.23**
Summer	OAC	140.29	1.3	1.66	63.37	**0.14**		0.08–0.24	**0.21**
		Simulated TGU Properties (CEN)	**1.13**			**0.19**			**0.346**

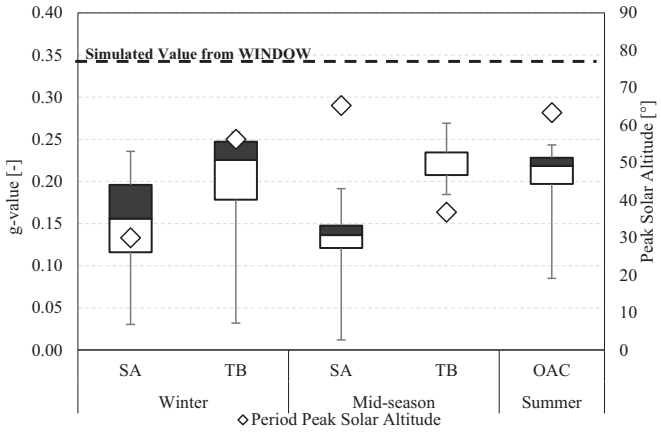


Fig. 6. Experimental effective g-values (boxplots) of the HHW under different operating modes (SA, TB, OAC) and seasonal conditions. The dashed line represents the simulated g-value obtained from WINDOW under perpendicular incidence. Diamonds indicate the peak solar altitude for each analysed period.

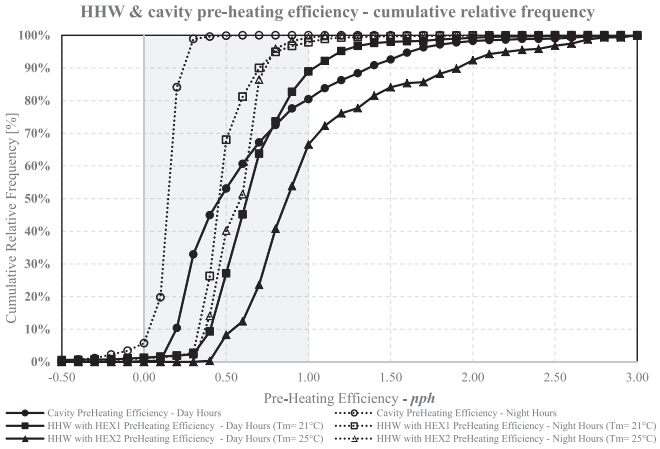


Fig. 7. Pre heating efficiency.

variation of the latter, emphasize the importance of dynamic effects, such as ventilation, in reducing solar heat transmission through ventilated façades. Therefore for these kind of systems, dynamic metrics should provide a better representation of the real-world energy performance of the HHW.

4.2. Dynamic key performance indicators

4.2.1. Seasonal performance / efficiencies

The following results are presented as cumulative frequency distributions, over the full monitoring period for each ventilation configuration. This approach shows the share of time during which specific efficiency levels are achieved or exceeded, capturing both typical and extreme conditions and providing a clear view of performance consistency over time.

4.2.1.1. HHW ventilated cavity performance. During the winter and mid-season, the HHW façade system operates mainly Supply Air (SA) and Thermal Buffer (TB). The SA strategy preheats ventilation air using solar radiation on the glazing, reducing ventilation heat losses and performing best under high solar irradiance.

Fig. 7, presents the cumulative frequency of the pre-heating efficiency for 35 days of winter at a constant airflow rate of 99.31 m^3/h per meter of façade. Although the airflow is continuous, thermocouples installed along its path allow the thermal contribution of the v-TGU and the a-PCM HEX to be quantified separately. This enables isolation of the added value of the a-PCM HEX compared to the cavity alone. Each curve distinguishes between daytime (solid lines, $I > 0$) and nighttime (dotted lines, $I = 0$) conditions. Pre-heating efficiency remains above zero for nearly 100% of the time, indicating continuous heat recovery. During daytime, the cavity alone achieves efficiencies above 1 for about 20% of the time, meaning that for 20% of time temperatures higher than the indoor set-point would be provided to the indoor environment. The median values around 0.60–0.65, meaning that ventilation losses are typically reduced by 60–65%. When the a-PCM HEX is included, peak efficiencies above 1 occur less frequently (<10%), but the median efficiency increases, indicating more stable and controlled heat recovery. At night, cavity performance drops significantly (often <0.3) due to limited thermal inertia of the cavity itself, which can only release residual heat stored during the previous hours. In contrast, the a-PCM HEX maintains efficiencies consistently above 0.4, as the stored latent heat is released when air temperatures fall below the PCM melting point. This demonstrates the HEX's key role in extending heat recovery beyond solar hours.

When the outdoor air temperatures and incident solar irradiance are low, SA mode becomes less effective, potentially leading to net energy losses if ventilation continues. Under these conditions, the optimal operational configuration for the HHW module is the TB strategy, which exploits the passive thermal buffering capabilities of the façade's ventilated cavity. Fig. 8 illustrates the cumulative frequency distribution of the thermal buffer efficiency, η_{TB}, assessed separately for daytime (solid line) and nighttime (dashed line) periods.

Considering daytime conditions (solid line), the graph shows that efficiency values exceed unity ($\eta_{TB} > 1$), representing periods of net heat gains for nearly 40% of the daytime hours, highlighting significant passive solar contributions, while for 50% of time a value of 0.8 is reached, indicating heat losses are reduced by 80% compared to the HHW without the cavity in thermal buffer mode. During nighttime (dashed line), the cumulative frequency indicates consistently lower values, with η_{TB} ranging between approximately 0.3 to 0.5 for most of the time, and an average of 0.40. The persistence of positive efficiency values, even at night, emphasizes the cavity's continued effectiveness in minimizing thermal losses by retaining on average 40% more heat compared to a double glazing unit with equivalent thermo-optical properties of the most internal two layers of the HHW.

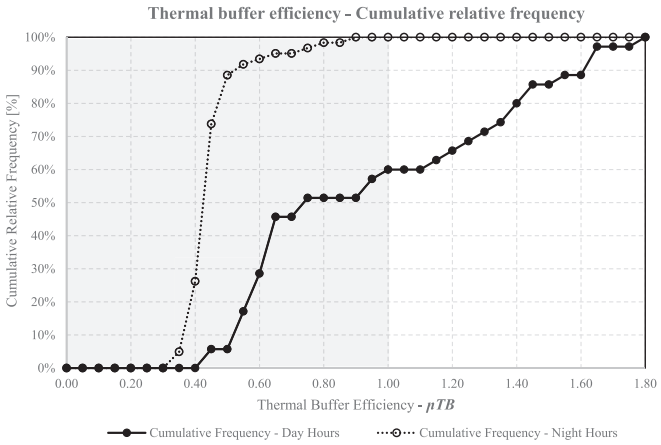


Fig. 8. Thermal buffer efficiency.

4.2.1.2. Dynamic insulation efficiency. Fig. 9 illustrates the cumulative frequency distribution of the Dynamic Insulation Efficiency for the HHW system operating in OAC mode. This KPI measures the cavity's capability to reduce incoming solar heat gains by means of cavity ventilation during the daytime, while increasing heat transfer during the nighttime. The distribution reveals that ε assumes positive values for over 90% of the monitored period. Average values are around 0.75 meaning that overall the cavity ventilation is able to remove about 75% of the absorbed solar radiation within the HHW system. This indicates that in most conditions, the cavity airflow effectively offsets a substantial portion of the combined transmission and solar gains, thereby contributing to thermal load reduction on the interior space. Notably, values of $\varepsilon > 1$ are also observed, for 20% of time, corresponding to periods where the ventilated cavity extracts more energy than the one that is entering through short-wave solar transmission, likely occurring during times of low solar radiation and favourable thermal gradients. The sharp rise in the cumulative curve between $\varepsilon = 0.6$ and $\varepsilon = 1$ confirms that the HHW façade frequently operates near peak dynamic insulation effectiveness. This high-efficiency range demonstrates the potential of the OAC strategy to maintain dynamic insulation performance across a range of environmental conditions.

Conversely, for approximately 10% of the time, ε falls below zero, indicating that the cavity may act as a heat sink rather than reducing heat losses. These instances likely align with early morning or night periods when radiative cooling causes the cavity to behave counterintuitively, increasing heat losses through the HHW.

4.2.1.3. Air-to-phase change material heat exchanger outlet temperatures.

When the façade operates in TB or OAC mode, the airflow supplied to the indoor environment is drawn directly from the outdoor environment through the a-PCM HEX. Fig. 10 presents the cumulative frequency distribution of the a-PCM HEX outlet temperatures during the heating period (TB mode). Distinguishing between daytime (solid lines) and nighttime (dashed lines) conditions. During daytime, only HEX2 is able to supply air temperature to the winter setpoint (≈20 °C) for roughly 30% of the time. For the remaining period, outlet temperatures consistently remain above outdoor air temperature, confirming active heat release from the HEX2 with PCM 25 °C. In contrast, the 21 °C PCM more frequently operates near or below its phase-change range, occasionally resulting in lower outlet temperatures due to partial charging. During nighttime, when outdoor temperatures decrease significantly, both PCMs continue to discharge stored heat, maintaining outlet temperatures above ambient conditions and extending thermal pre-conditioning beyond solar hours. HEX2, in particular, provides a more evident temperature increase, as it stores a greater amount of heat during daytime.

Fig. 11 presents the cumulative frequency distribution of the a-PCM HEX outlet temperatures during the cooling period. During daytime, both HEX configurations reduce the supply air temperature compared to outdoor conditions, with HEX2 showing particularly strong performance. While outdoor air frequently exceeds 30 °C, the outlet temperature after HEX2 (Tm = 25 °C) is generally maintained below 26 °C, demonstrating effective cooling through latent heat absorption. During nighttime, as outdoor temperatures decrease, the outlet temperatures of both HEXs remain slightly above outdoor levels, indicating heat release from the energy stored during daytime. Despite this discharge phase, the system maintains air temperatures within a tolerable range, typically below 28 °C.

4.2.2. HHW performance in design days

To better understand the behaviour of the HHW and evaluate its thermal performance across varying seasons and operation modes, an energy balance analysis was conducted on representative typical days, according to Section 3.3. The selected days are characterized by either average or peak seasonal conditions for the climate of Turin. In this paragraph, three representative peak typical days and average typical days from the experimental campaign are presented, each couple corresponding to a different season. Table 6 shows the climatic boundary conditions of the typical days presented in the next paragraphs.

4.2.2.1. Winter season – thermal buffer operational mode. Fig. 12 illustrates the thermal buffer (TB) configuration on 25/02/2024. In this mode, the cavity vents remain closed and the cavity acts as a passive buffer zone. Outdoor air is supplied directly to the PCM heat exchanger and then introduced indoors, so the outlet temperature depends

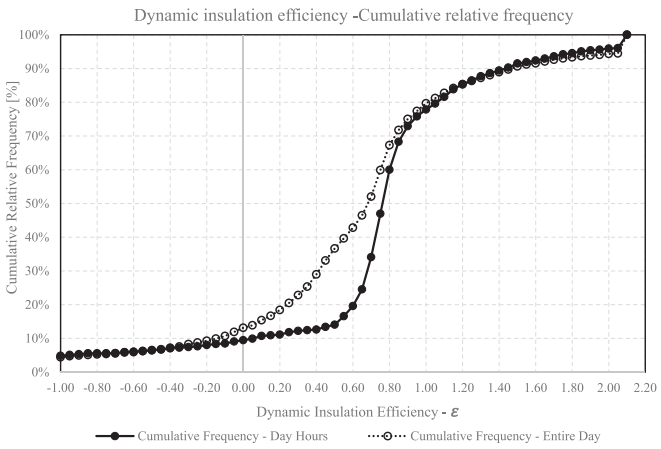


Fig. 9. Dynamic insulation efficiency.

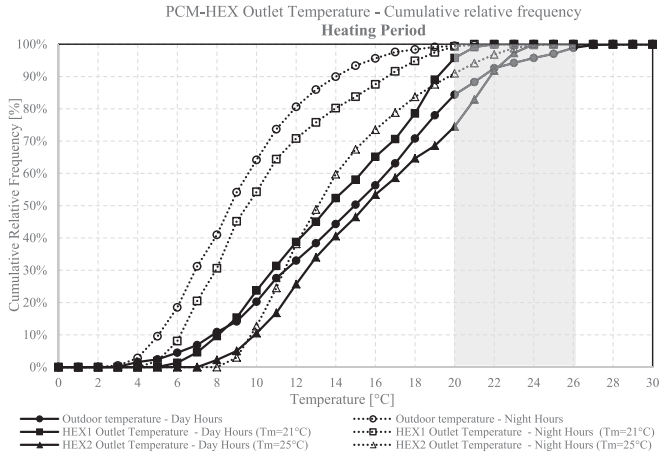


Fig. 10. a-PCM HEX and outdoor air temperatures during the heating period.

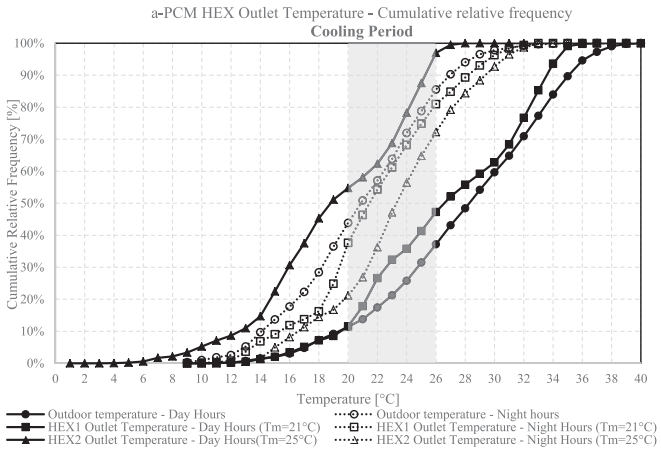


Fig. 11. a-PCM HEX and outdoor air temperatures during the cooling period.

exclusively on the PCM's capacity to store and release heat. This strategy is particularly suitable under low solar radiation, when cavity air temperatures cannot approach the indoor setpoint. In such conditions, keeping the cavity closed limits ventilation heat losses and may allow limited conductive heat transfer toward the indoor side. On this day, the average outdoor temperature was 7.6 °C and the cumulative solar radiation reached 3186 Wh/m^2. The air mass flow rate was reduced to 49.7 m^3/h, significantly affecting heat exchange within the HEX. As shown in the figure, the HEX outlet temperature increased only moderately during solar hours, reaching approximately 18–20 °C. The PCM thermal energy curve indicates partial charging between 11:00 and 14:00, followed by rapid discharge once solar input decreased. The limited solar gains and reduced airflow constrained convective heat exchange, resulting in a mainly stabilizing effect rather than substantial air pre-heating. Under these boundary conditions, the TB mode primarily mitigated temperature fluctuations, with the PCM acting as a short-term thermal reservoir rather than a strong pre-heating source.

4.2.2.2. Mid-season – supply-air operational mode. Fig. 13 shows the energy balance and temperature evolution for 12/05/2024, representative of mid-season operation in Supply Air (SA) mode. The day was characterized by an average outdoor temperature of 20.2 °C and a cumulative solar radiation of approximately 2989 Wh/m^2, under average seasonal conditions. This pronounced diurnal variation, combined with the presence of solar radiation, allows the air exiting the cavity to exchange significant amounts of energy with the PCM. At night, the PCM releases the energy stored during the day, heating the supply air to around 17 °C, values closer to the indoor setpoint temperature (23 °C). Conversely, during the day, the PCM charges, absorbing heat from the incoming air (visible as the negative PCM thermal energy in the graph). This cyclical process effectively enables the PCM to store excess thermal energy during the day and reutilize it during the following night, contributing to both thermal comfort stabilization and improved energy efficiency of the HHW façade system.

4.2.2.3. Summer season – outdoor-air curtain operational mode. In cooling dominated period, the HHW operates in Outdoor Air Curtain (OAC)

Table 6
Climatic boundary conditions of typical days.

		UNI 10349					Measured		
		T Average [°C]	T peak [°C]	H [Wh/m^2]	Typical Day [dd/mm/yyyy]	Operational Mode	T average [°C]	T peak [°C]	H [Wh/m^2]
	Peak		−8	0	1/9/2024	SA	–	4.35	0
					26/02/2024	TB	–	4.00	122
	Average	3.2		3000	2/2/2024	SA	6.70		4574
Winter					25/02/2024	TB	7.60		3186
		21.1		2639	12/05/202024	SA	20.17	–	2989
Mid-Season	Average	16.7		2722	18/10/2024	TB	16.20	–	2171
		18.8		3111	–	–	–	–	–
	Peak		30.7	3635	21/08/2024	OAC	–	35.45	4339
Summer	Average	23.3		2944	27/08/2024	OAC	24.18	–	2755

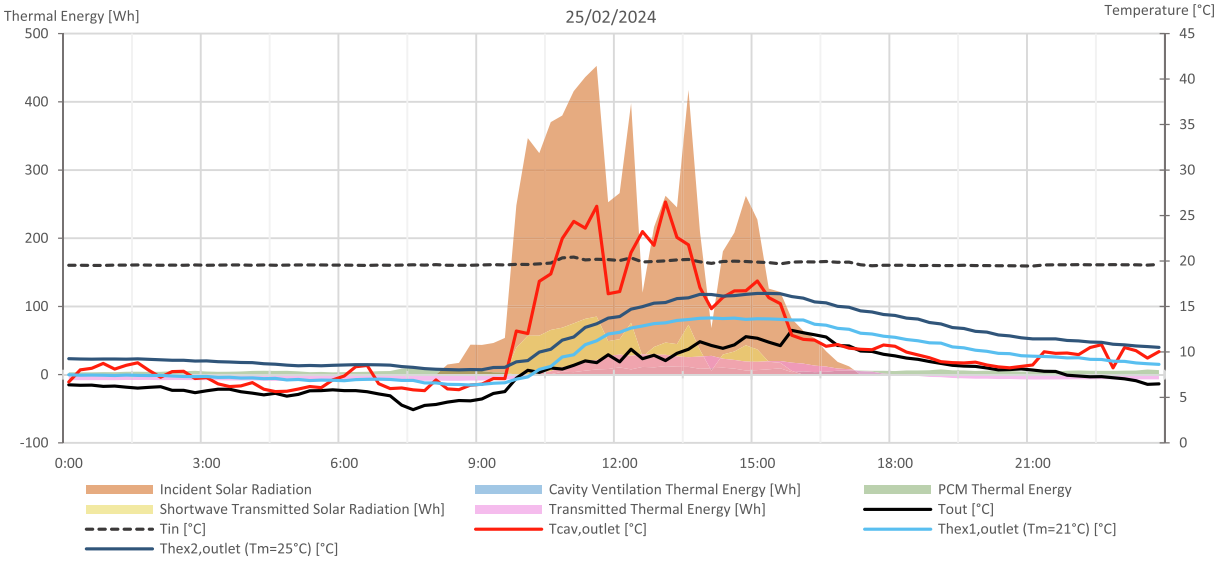


Fig. 12. Winter Typical day - Thermal buffer.

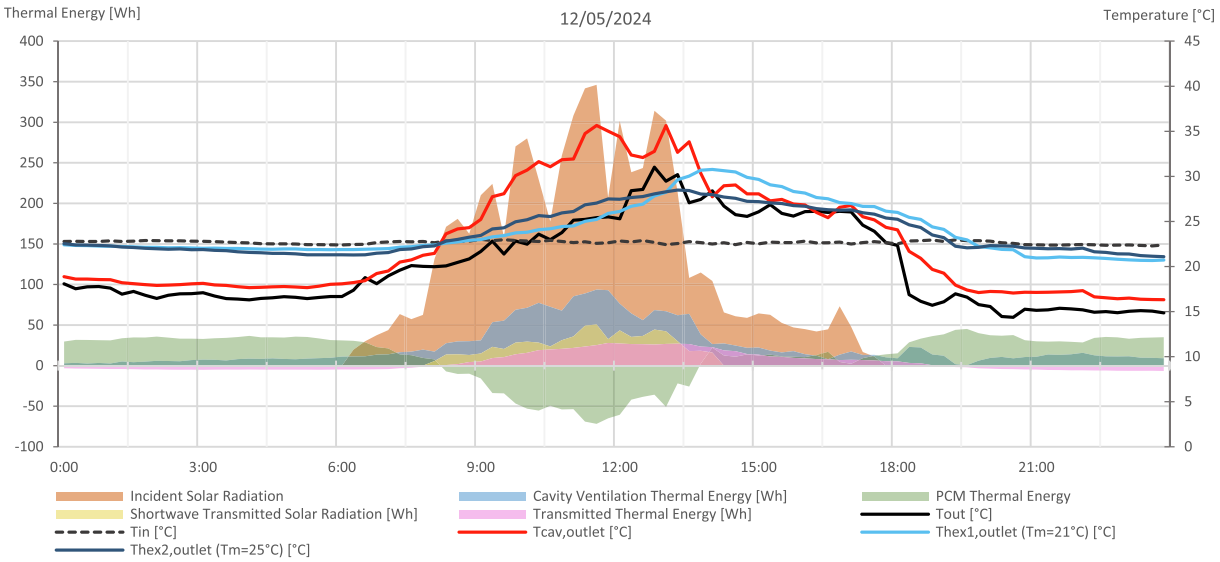


Fig. 13. Mid-season Typical day - Supply Air.

mode, exhausting solar-heated cavity air outdoors while supplying fresh air directly from the exterior through the a-PCM HEX. The 21st of August 2024 (Fig. 14) was characterized by peak outdoor temperatures up to 36 °C and high cumulative solar radiation (4340 Wh/m^2). Solar gains significantly increased cavity thermal energy during the central hours of the day; however, this heat was expelled through cavity ventilation, limiting its transmission indoors. The PCM contribution was moderate under these conditions. In the morning (approximately 6:00–11:00), as outdoor temperatures exceeded 20 °C, the PCM began melting and absorbed heat from the incoming air, providing pre-cooling of about 4 °C. After 11:00, as outdoor temperatures rose toward 30–33 °C, the HEX outlet temperatures progressively approached outdoor values, indicating that the PCM had reached its storage capacity. Between 11:00 and 16:00, limited temperature reduction was observed. In the late afternoon, as temperatures decreased, partial PCM solidification occurred, briefly restoring a small pre-cooling effect (about 4–5 °C). During nighttime hours, the release of stored heat led to a slight increase (1–2 °C) in supply air temperature. Overall, under high solar radiation and elevated airflow, the OAC configuration effectively rejected solar gains through cavity ventilation. The a-PCM HEX provided additional air temperature moderation, although its cooling contribution remained limited under peak summer conditions.

4.2.3. *TGU vs. HHW energy performance comparison*

Fig. 15 compares the daily net thermal energy exchanged with the indoor environment for the HHW and for the two reference TGU configurations. Each group of bars corresponds to one representative experimental day, selected to describe either peak or average seasonal boundary conditions under a specific operating mode. The date is reported on the x-axis, while the corresponding operating strategy is indicated below each group: Supply Air (SA), Thermal Buffer (TB), or Outdoor Air Curtain (OAC). Positive values indicate heat gains toward the indoor environment, whereas negative values indicate heat losses from the indoor environment. The three bars within each group refer to the TGU, the TGU-benchmark, and the HHW, respectively. All systems were compared under the same indoor temperature setpoint and the same ventilation airflow rate. The cross markers indicate the daily cumulative incident solar radiation and refer to the secondary y-axis. Under winter SA operation, the HHW shows a strong reduction in total heat losses compared to both TGUs, reaching up to 90% lower losses

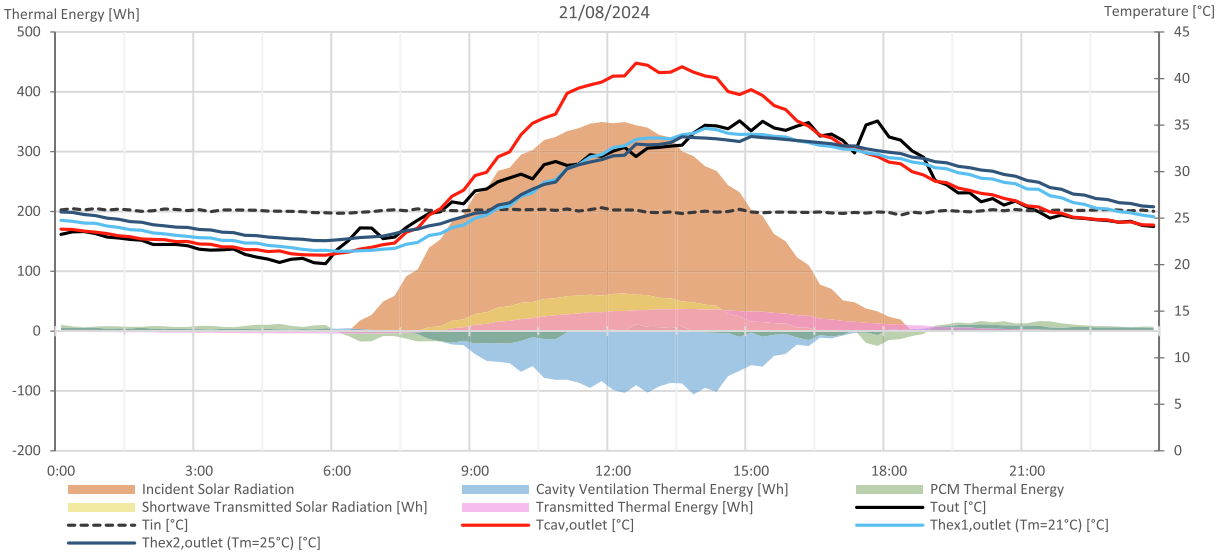


Fig. 14. Summer Typical day - Outdoor air curtain.

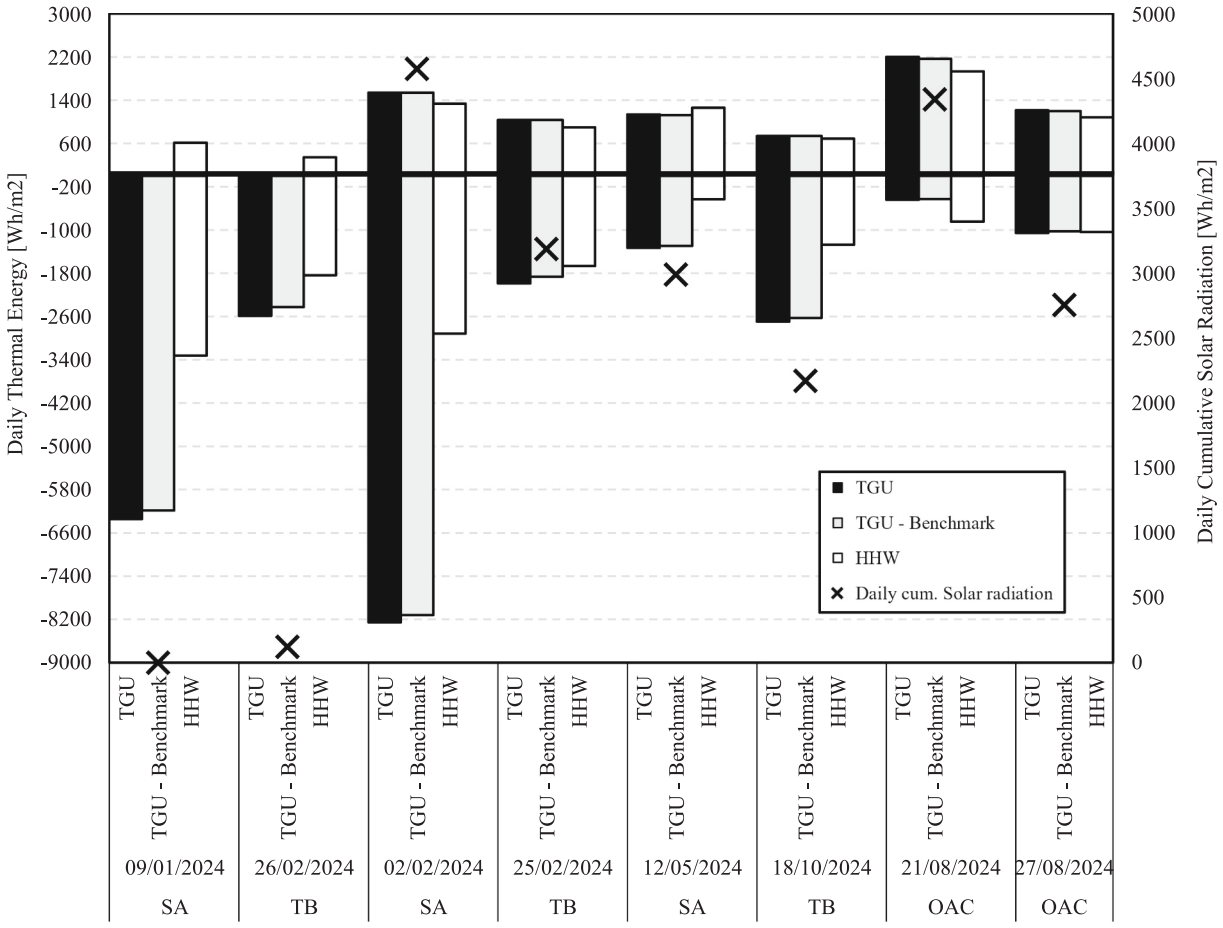


Fig. 15. Daily net thermal energy exchanged with the indoor environment for the HHW, TGU, and TGU-benchmark under representative seasonal days and operating modes. Positive and negative values indicate heat gains and losses, respectively. Cross markers refer to daily cumulative incident solar radiation on the secondary y-axis.

despite its higher static U-value (1.90 W/(m^{2}K)). This improvement is primarily due to the reduction of ventilation heat losses and the elevated cavity air temperature, which decreases conductive heat transfer. Since the shortwave transmittance is identical across systems, the differences observed in total gains are mainly attributable to longwave exchanges and to the portion of absorbed solar energy converted into useful preheating of ventilation air within the cavity and a-PCM HEX. The TGU exhibits higher net losses, while the TGU-benchmark performs slightly better but remains significantly inferior to the HHW under SA operation. In TB mode under similar boundary conditions, the absence of ventilation heat recovery reduces the performance gap, leading to smaller reductions in losses relative to the TGUs.

During mid-season representative days, HHW in SA strategy is able to achieve a similar reduction of heat losses compared to the TGUs as compared to a winter scenario, due to a similar magnitude of reduction of ventilation heat losses. On the other side, due to the high temperatures achieved in the cavity, less reduction of heat gains is achievable compared to the heating dominated conditions, hence comparatively higher long-wave heat gains. When adopting TB operational mode, provided the fact that the preheated cavity ventilation is not adopted to offset the ventilation heat gains and losses of the indoor environment, higher heat losses and much lower heat gains are achieved compared to the SA mode in the same season (and compared to the reference TGUs).

Under cooling-dominated conditions, the OAC configuration enables the HHW to expel solar-heated cavity air outdoors. This results, for an average summer day, in lower heat gains, due to lower transmission due to lower cavity temperatures, and primarily to much lower long-wave solar radiation heat gains (due to the impact of the ventilated cavity). These improvements result from the dynamic insulation effect provided by the ventilated cavity, which expels excess heat before it reaches the indoor environment, and from the PCM's modest pre-cooling contribution during the early part of the day. On the other side, the a-PCM HEX slightly reduces ventilation heat gains, while consequentially also reduces heat losses, due to higher temperature of the ventilation air during the night time after regenerating the PCM, compared to the TGU.

Overall, HHW consistently outperforms both TGUs in reducing both heat gains and losses, also considering ventilation heat losses / gains, mainly by converting solar energy into higher temperature of the ventilated cavity, that can be then effectively used in the indoor space also to offset ventilation energy needs (making use of the PCM latent heat storage capacity) or be expelled to the outdoor (in cooling dominated scenario).

5. Conclusion

This paper presented the experimental characterization of the energy performance of the Heat Harvesting Window prototype, developed in the context of the H2020 European project iclimabuilt [40]. The HHW is an innovative ventilated window, integrating a TGU with outer ventilated cavity with an air to PCM heat exchanger. The system was developed to address current limitations in conventional transparent envelope components, enhancing building energy performance by increasing solar energy to heat conversion, minimizing transmission and ventilation heat losses, while continuously providing outdoor fresh air, and reducing summer solar heat gains.

A mock-up of HHW prototype was installed and tested under diverse

seasonal conditions and operational strategies on an outdoor test facility in Turin, enabling a comprehensive characterization of its behaviour through both standardized and innovative dynamic performance metrics.

The experimental results of the static KPIs revealed that when the cavity is ventilated, the system exhibits a higher U-value and a significantly lower g-value and lower solar transmittance τ_{sol}. For example, the measured U-value ranged from approximately 1.0–1.2 W/(m^2K)under Thermal Buffer conditions to about 1.9 W/(m^2K)in Supply Air mode, while the effective g-value ranged between approximately 0.12 and 0.23, remaining below the simulated static value of 0.346. While such static indicators are useful for comparing with conventional glazing systems, they fall short in capturing the actual energy performance of advanced façade components like HHW. On the other side, the dynamic KPIs clearly demonstrate that the cavity alone provides thermal buffering and insulation benefits, but its performance is greatly enhanced when coupled with air to PCM heat exchanger, in order to offset ventilation energy needs. The PCM module not only extends heat recovery into low-radiation periods but also improves seasonal adaptability by contributing to both pre-heating and pre-cooling depending on the boundary conditions.

To further understand HHW's seasonal behaviour, an energy balance analysis was performed on representative design days for winter, mid-season and summer conditions, and compared to an equivalent TGU and market-like TGU, in terms of impact to the indoor environment. The experimental investigation showed that the HHW demonstrated substantial advantages in all modes, providing dynamic insulation during summer, pre-heating and thermal buffering in winter and transitional periods. Compared to a TGU, in SA and TB mode although lower heat gains are obtained in winter and mid-season, 80–90% lower heat losses are obtained (mainly due to reduction in ventilation heat losses), whose magnitude is 3–4 times the one of the heat gains in typical days. Moreover during summer, OAC operations allows a reduction of more than 40% of heat gains, driven mainly by dynamic insulation and limited air pre-cooling provided by the a-PCM HEX. While TGU offers high performances, but in a passive way, HHW strength lies in its adaptability and active thermal management across diverse climate conditions. Overall, the HHW façade demonstrated promising thermal responsiveness, operational flexibility, and energy-saving potential under the tested conditions. These results support its further development as a climate-adaptive transparent façade concept, although additional studies are required to assess its scalability, whole-building integration, indoor air quality implications.

The findings of this study should be interpreted within the boundaries of the experimental configuration. The prototype was tested as a single South-oriented façade module under the temperate climatic conditions of Turin; therefore, further investigations are required to assess the performance of the HHW under different orientations, climates, façade geometries, control strategies, and building uses. In addition, although the system was operated with measured airflow rates compatible with continuous fresh-air supply, indoor air quality compliance was not directly assessed in this study. No measurements of CO_2 concentration, pollutants, or occupancy-related IAQ indicators were included. Consequently, the results demonstrate the ventilation and thermal pre-conditioning potential of the system, but not its full IAQ performance.

CRediT authorship contribution statement

Ginevra Li Castri: Writing – review & editing, Writing – original draft, Visualization, Methodology, Investigation, Formal analysis, Data curation. **Aseel Raad:** Writing – review & editing, Writing – original draft, Visualization, Methodology, Formal analysis, Data curation. **Lorenzo Rapone:** Methodology, Data curation, Conceptualization. **Valentina Serra:** Resources, Methodology, Conceptualization. **Fabio Favoino:** Writing – review & editing, Writing – original draft, Supervision, Resources, Project administration, Methodology, Funding acquisition, Conceptualization.

Declaration of competing interest

The authors declare that they have no known competing financial interests or personal relationships that could have appeared to influence the work reported in this paper.

Acknowledgements

The activities presented in this paper were carried out as part of the H2020 project “iClimabuilt - Functional and advanced insulating and energy harvesting/storage materials across climate adaptive building envelopes” (Grant Agreement no. 952886). We acknowledge the work of Asmaa Ali (Rubitherm Technologies GmbH), Gianni Cassera and Anna Bogacz (BGTeC s.p. zo.o.), and Iñaki García (CIDETEC) for helping in developing the design and operations of the HHW mock-up. Moreover authors are grateful to the student Marco Lavilletta for the help with the experimental campaign.

Appendix A. Appendix

Table A.1
Daily climate boundary conditions and energy balance terms for the representative winter, mid-season and summer days analysed. Results are reported for the reference TGU, the TGU benchmark and the HHW prototype under the selected operating strategies, namely Supply Air (SA), Thermal Buffer (TB) and Outdoor Air Curtain (OAC).

			Winter				Mid-season		Summer - Peak Days	
			Peak Days		Average Days		Average Days		Peak Days	Average Days
Climate Boundary Conditions			SA 09/01/2024	TB 26/02/2024	SA 02/02/2024	TB 25/02/2024	SA 12/05/2024	TB 18/10/2024	OAC 21/08/2024	OAC 27/08/2024
Temperature	Daily Range	[°C]	2.4–5.9	3.0–6.4	0.5–15.8	3.6–12.4	14.4–31.0	13.5–22.4	20.1–35.4	17.5–32.06
	Average	[°C]	4.4	4.0	6.7	7.6	20.2	16.2	27.5	24.2
Irradiance	Daily Total	[Wh/m2]	0	122	4574	3186	2989	2171	4339	2755
TGU	Q_{sw}^{TGU}	[Wh/m^2]	0.00	0.00	827.82	535.07	282.73	397.65	552.20	383.49

(*continued on next page*)

Table A.1 (*continued*)

			Winter				Mid-season		Summer - Peak Days	
	Q_{tr}^{TGU-}	[Wh/m^2]	−413.34	−424.03	−350.84	−326.14	−98.27	−174.51	−35.73	−86.95
	Q_{tr}^{TGU+}	[Wh/m^2]	0.00	0.00	0.00	0.00	30.72	0.00	82.39	34.51
	Q_{lw}^{TGU}	[Wh/m^2]	0.00	19.04	713.47	496.99	466.36	338.67	676.96	429.74
	Q_{vent}^{TGU+}	[Wh/m^2]	0.00	0.00	0.00	0.00	357.11	0.00	886.50	365.15
	Q_{vent}^{TGU-}	[Wh/m^2]	−5930.78	−2164.13	−7902.39	−1661.09	−1231.62	−2519.01	−405.19	−969.54
	Q +	[Wh/m^2]	**0.00**	**19.04**	**1541.29**	**1032.06**	**1136.92**	**736.32**	**2198.04**	**1212.88**
	Q -	[Wh/m^2]	**−6344.12**	**−2588.17**	**−8253.23**	**−1987.23**	**−1329.89**	**−2693.52**	**−440.93**	**−1056.48**
	$Q_{sw}^{TGUbencmark}$	[Wh/m^2]	0.00	0.00	827.82	535.07	282.73	397.65	552.20	383.49
	$Q_{tr}^{TGUbenchmark-}$	[Wh/m^2]	−256.05	−262.67	−217.34	−202.04	−60.87	−108.10	−22.14	−53.86
	$Q_{tr}^{TGUbenchmark+}$	[Wh/m^2]	0.00	0.00	0.00	0.00	19.03	0.00	51.04	21.38
TGU - Benchmark	$Q_{lw}^{TGUbenchmark}$	[Wh/m^2]	0.00	19.04	713.47	496.99	466.36	338.67	676.96	429.74
	$Q_{vent}^{TGUbenchmark+}$	[Wh/m^2]	0.00	0.00	0.00	0.00	357.11	0.00	886.50	365.15
	$Q_{vent}^{TGUbenchmark-}$	[Wh/m^2]	−5930.78	−2164.13	−7902.39	−1661.09	−1231.62	−2519.01	−405.19	−969.54
	Q +	[Wh/m^2]	**0.00**	**19.04**	**1541.29**	**1032.06**	**1125.23**	**736.32**	**2166.69**	**1199.75**
	Q -	[Wh/m^2]	**−6186.83**	**−2426.81**	**−8119.72**	**−1863.12**	**−1292.49**	**−2627.12**	**−427.33**	**−1023.40**
	Q_{sw}^{HHW}	[Wh/m^2]	0.00	0.00	828.24	528.13	316.95	408.72	589.14	403.60
	Q_{tr}^{HHW-}	[Wh/m^2]	0.00	0.00	−126.64	−255.07	−280.60	−208.24	−490.23	−254.69
	Q_{tr}^{HHW+}	[Wh/m^2]	612.50	345.41	400.06	215.45	106.91	94.83	91.11	91.11
	Q_{lw}^{HHW}	[Wh/m^2]	0.00	0.00	34.54	155.69	287.16	186.52	410.04	235.91
HHW	Q_{vent}^{HHW+}	[Wh/m^2]	0.00	0.00	74.18	0.00	548.34	0.00	841.62	350.81
	Q_{vent}^{HHW-}	[Wh/m^2]	−3322.94	−1837.37	−2789.19	−1411.75	−149.35	−1064.38	−354.56	−782.12
	Q +	[Wh/m^2]	**612.50**	**345.41**	**1337.02**	**899.27**	**1259.36**	**690.07**	**1931.91**	**1081.42**
	Q -	[Wh/m^2]	**−3322.94**	**−1837.37**	**−2915.83**	**−1666.83**	**−429.95**	**−1272.62**	**−844.79**	**−1036.81**

Data availability

Data will be made available on request.

References

[1] European Parliament And The Council, Directive (EU) 2023/1791 of the European Parliament and of the Council of 13 September 2023 on energy efficiency and amending Regulation (EU) 2023/955 (recast) (Text with EEA relevance), 2023.

[2] Q. Jin, M. Overend, Sensitivity of façade performance on early-stage design variables, Energ. Buildings 77 (2014) 457–466, https://doi.org/10.1016/j.enbuild.2014.03.038.

[3] F. Favoino, R.C.G.M. Loonen, M. Michael, G. De Michele, S. Avesani, Advanced fenestration—technologies, performance and building integration, in: Rethinking Building Skins: Transformative Technologies and Research Trajectories, Elsevier, 2021, pp. 117–154, https://doi.org/10.1016/B978-0-12-822477-9.00038-3.

[4] X. Zhao, A. Wei, S. Zou, Q. Dong, J. Qi, Y. Song, et al., Controlling naturally ventilated double-skin façade to reduce energy consumption in buildings, Renew. Sustain. Energy Rev. 202 (2024), https://doi.org/10.1016/j.rser.2024.114649.

[5] X. Liu, C. Shen, J. Wang, C. Zhang, Y. Shuai, Static and dynamic regulations of photovoltaic double skin facades towards building sustainability: a review, Renew. Sustain. Energy Rev. 183 (2023), https://doi.org/10.1016/j.rser.2023.113458.

[6] P.C. Wong, D. Prasad, M. Behnia, A new type of double-skin façade configuration for the hot and humid climate, Energ. Buildings 40 (2008) 1941–1945, https://doi.org/10.1016/j.enbuild.2008.04.014.

[7] G. Gennaro, E. Catto Lucchino, F. Goia, F. Favoino, Modelling double skin façades (DSFs) in whole-building energy simulation tools: validation and inter-software comparison of naturally ventilated single-story DSFs, Build. Environ. 231 (2023), https://doi.org/10.1016/j.buildenv.2023.110002.

[8] E. Catto Lucchino, G. Gennaro, F. Favoino, F. Goia, Modelling and validation of a single-storey flexible double-skin façade system with a building energy simulation tool, Build. Environ. 226 (2022), https://doi.org/10.1016/j.buildenv.2022.109704.

[9] K. Pelletier, C. Wood, J. Calautit, Y. Wu, The viability of double-skin façade systems in the 21st century: a systematic review and meta-analysis of the nexus of factors affecting ventilation and thermal performance, and building integration, Build. Environ. 228 (2023), https://doi.org/10.1016/j.buildenv.2022.109870.

[10] K.A.R. Ismail, J.R. Henríquez, Two-dimensional model for the double glass naturally ventilated window, Int. J. Heat Mass Transf. 48 (2005) 461–475, https://doi.org/10.1016/j.ijheatmasstransfer.2004.09.022.

[11] Y. Hu, R. Guo, P.K. Heiselberg, Performance and control strategy development of a PCM enhanced ventilated window system by a combined experimental and numerical study, Renew. Energy 155 (2020) 134–152, https://doi.org/10.1016/j.renene.2020.03.137.

[12] C. Aparicio-Fernández, J.L. Vivancos, P. Ferrer-Gisbert, R. Royo-Pastor, Energy performance of a ventilated façade by simulation with experimental validation, Appl. Therm. Eng. 66 (2014) 563–570, https://doi.org/10.1016/j.applthermaleng.2014.02.041.

[13] K.A.R. Ismail, T.G.S. Lago, F.A.M. Lino, M.V. Mondlane, M.P.R. Teles, Experimental investigation on ventilated window with reflective film and development of correlations, Sol. Energy 230 (2021) 421–434, https://doi.org/10.1016/j.solener.2021.10.061.

[14] I. Khalifa, L. Gharbi-Ernez, E. Znouda, C. Bouden, Assessment of the Inner Skin Composition Impact on the Double-skin Façade Energy Performance in the Mediterranean Climate. Energy Procedia 111, Elsevier Ltd, 2017, pp. 195–204, https://doi.org/10.1016/j.egypro.2017.03.021.

[15] A. Alberto, N.M.M. Ramos, R.M.S.F. Almeida, Parametric study of double-skin facades performance in mild climate countries, J. Build. Eng. 12 (2017) 87–98, https://doi.org/10.1016/j.jobe.2017.05.013.
[16] Y. Li, J. Darkwa, G. Kokogiannakis, W. Su, Effect of design parameters on thermal performance of integrated phase change material blind system for double skin façade buildings, Int. J. Low-Carbon Technol. 14 (2019) 286–293, https://doi.org/10.1093/ijlct/ctz010.
[17] M.M.S. Ahmed, A. Radwan, A.A. Serageldin, A. Abdeen, E.M. Abo-Zahhad, K. Nagano, The thermal potential of a new multifunctional sliding window, Solar Energy 226 (2021) 389–407, https://doi.org/10.1016/j.solener.2021.08.045.
[18] R. Koželj, U. Mlakar, E. Zavrl, U. Stritih, R. Stropnik, An experimental and numerical analysis of an improved thermal storage tank with encapsulated PCM for use in retrofitted buildings for heating, Energy Build. 248 (2021), https://doi.org/10.1016/j.enbuild.2021.111196.
[19] A. kumar Dubey, J. Sun, T. Choudhary, M. Dash, D. Rakshit, M.Z. Ansari, et al., Emerging phase change materials with improved thermal efficiency for a clean and sustainable environment: an approach towards net zero, Renew. Sustain. Energy Rev. 182 (2023), https://doi.org/10.1016/j.rser.2023.113421.
[20] S. Grynning, F. Goia, B. Time, Dynamic thermal performance of a PCM window system: characterization using large scale measurements, Energy Procedia 78 (2015) 85–90, https://doi.org/10.1016/j.egypro.2015.11.119.
[21] F. Goia, E. Boccaleri, Physical-chemical properties evolution and thermal properties reliability of a paraffin wax under solar radiation exposure in a real-scale PCM window system, Energ. Buildings 119 (2016) 41–50, https://doi.org/10.1016/j.enbuild.2016.03.007.
[22] G. Wang, Y. Ma, S. Zhang, D. Li, R. Hu, Y. Zhou, Thermal performance of a novel double-glazed window combining PCM and solar control glass in summer, Renew. Energy 219 (2023) 119363, https://doi.org/10.1016/j.renene.2023.119363.
[23] H. Tang, Q. Long, C. Li, C. Li, Experimental study of a PV-PCM window under hot summer and warm winter climate, J. Energy Storage 96 (2024), https://doi.org/10.1016/j.est.2024.112724.
[24] F. Goia, M. Perino, V. Serra, Improving thermal comfort conditions by means of PCM glazing systems, Energ. Buildings 60 (2013) 442–452, https://doi.org/10.1016/j.enbuild.2013.01.029.
[25] F. Goia, M. Perino, V. Serra, Experimental analysis of the energy performance of a full-scale PCM glazing prototype, Solar Energy 100 (2014) 217–233, https://doi.org/10.1016/j.solener.2013.12.002.
[26] N. Ziasistani, F. Fazelpour, Comparative study of DSF, PV-DSF and PV-DSF/PCM building energy performance considering multiple parameters, Solar Energy 187 (2019) 115–128, https://doi.org/10.1016/j.solener.2019.05.040.
[27] Y. Li, W. He, W. Tao, C. Yang, Y. Li, J. Darkwa, Impacts of design parameters on the thermal performance of a macro-encapsulated phase-change-material blind integrated in a double-skin façade system, Energies 18 (2025), https://doi.org/10.3390/en18133326.
[28] Y. Li, S. Fu, Y. Li, Y. Peng, C. Yang, W. Tao, et al., Seasonal thermal performance of a macro-encapsulated phase change material blind integrated double skin façade system: an experimental study, Energ. Build. 325 (2024), https://doi.org/10.1016/j.enbuild.2024.114952.
[29] A. de Gracia, L. Navarro, A. Castell, Á. Ruiz-Pardo, S. Alvárez, L.F. Cabeza, Experimental study of a ventilated facade with PCM during winter period, Energ. Buildings 58 (2013) 324–332, https://doi.org/10.1016/j.enbuild.2012.10.026.
[30] A. De Gracia, L. Navarro, A. Castell, Á. Ruiz-Pardo, S. Álvarez, L.F. Cabeza, Thermal analysis of a ventilated facade with PCM for cooling applications, Energ. Buildings 65 (2013) 508–515, https://doi.org/10.1016/j.enbuild.2013.06.032.
[31] Y. Hu, P.K. Heiselberg, R. Guo, Ventilation cooling/heating performance of a PCM enhanced ventilated window - an experimental study, Energ. Build. 214 (2020), https://doi.org/10.1016/j.enbuild.2020.109903.
[32] V. Serra, F. Zanghirella, M. Perino, Experimental evaluation of a climate façade: energy efficiency and thermal comfort performance, Energ. Buildings 42 (2010) 50–62, https://doi.org/10.1016/j.enbuild.2009.07.010.
[33] F. Goia, V. Serra, Analysis of a non-calorimetric method for assessment of in-situ thermal transmittance and solar factor of glazed systems, Solar Energy 166 (2018) 458–471, https://doi.org/10.1016/j.solener.2018.03.058.
[34] F. Favoino, F. Goia, M. Perino, V. Serra, Experimental assessment of the energy performance of an advanced responsive multifunctional façade module, Energ. Buildings 68 (2014) 647–659, https://doi.org/10.1016/j.enbuild.2013.08.066.
[35] F. Favoino, F. Goia, M. Perino, V. Serra, Experimental analysis of the energy performance of an ACTive, RESponsive and solar (ACTRESS) façade module, Solar Energy 133 (2016) 226–248, https://doi.org/10.1016/j.solener.2016.03.044.
[36] L. Bianco, Y. Cascone, S. Avesani, P. Vullo, T. Bejat, R. Loonen, et al., Towards new metrics for the characterisation of the dynamic performance of adaptive façade systems, J. Facade Des. Eng. 6 (2018) 175–196, https://doi.org/10.7480/jfde.2018.3.2564.
[37] S.P. Corgnati, M. Perino, V. Serra, Experimental assessment of the performance of an active transparent façade during actual operating conditions, Solar Energy (2007), https://doi.org/10.1016/j.solener.2006.12.004.
[38] G. Li Castri, B. Manuela, F. Fabio, S. Valentina, P. Marco, Energy Performance Assessment of an Innovative Double-Skin façade with Air-PCM Heat Exchanger, 2024, https://doi.org/10.1007/978-981-97-8305-2_60.
[39] R. Lorenzo, L.C. Ginevra, L. Marco, F. Fabio, P. Marco, S. Valentina, Double-Skin façade with Air-PCM Latent Heat Exchanger: First Results from Experimental Campaign, 2026, https://doi.org/10.1007/978-981-97-8305-2_61.
[40] European funded project iclimabuilt. https://iclimabuilt.eu/, 2026.
[41] C. Barreneche, M.E. Navarro, L.F. Cabeza, A.I. Fernández, New database to select phase change materials: chemical nature, properties, and applications, J. Energy Storage 3 (2015) 18–24, https://doi.org/10.1016/j.est.2015.08.003.
[42] Italian organisation for Stardardisation (UNI), UNI 10349-1:2016, 2026.
[43] F. Di Mario, A. van Paassen, Modelling the air infiltrations in the second skin facade. Roceedings of the 4th International Conference on Indoor Air Quality, Ventilation and Energy Conservation in Buildings, October 2–5, City University of Hong Kong, 2001, pp. 873–880.
[44] Robin Mitchell, Christian Kohler, Dragan Curcija, Ling Zhu, Simon Vidanovic, Stephen Czarnecki, et al., WINDOW 7 User Manual, Berkeley, California, 2019.